



RELICS: Reionization Lensing Cluster Survey

Dan Coe¹, Brett Salmon¹, Maruša Bradač², Larry D. Bradley¹, Keren Sharon³, Adi Zitrin⁴, Ana Acebron⁴, Catherine Cerny⁵, Nathália Cibirka⁴, Victoria Strait², Rachel Paterno-Mahler³, Guillaume Mahler³, Roberto J. Avila¹, Sara Ogaz¹, Kuang-Han Huang², Debora Pelliccia^{2,6}, Daniel P. Stark⁷, Ramesh Mainali⁷, Pascal A. Oesch^{8,9}, Michele Trenti^{10,11}, Daniela Carrasco¹⁰, William A. Dawson¹², Steven A. Rodney¹³, Louis-Gregory Strolger¹, Adam G. Riess¹, Christine Jones¹⁴, Brenda L. Frye⁷, Nicole G. Czakon¹⁵, Keiichi Umetsu¹⁵, Benedetta Vulcani¹⁶, Or Graur^{14,17,35}, Saurabh W. Jha¹⁸, Melissa L. Graham¹⁹, Alberto Molino^{20,21}, Mario Nonino²², Jens Hjorth²³, Jonatan Selsing^{9,24}, Lise Christensen²³, Shotaro Kikuchihara^{25,26}, Masami Ouchi^{25,27}, Masamune Oguri^{27,28,29}, Brian Welch³⁰, Brian C. Lemaux², Felipe Andrade-Santos¹⁴, Austin T. Hoag², Traci L. Johnson³¹, Avery Peterson³¹, Matthew Past³¹, Carter Fox³, Irene Agulli⁴, Rachael Livermore^{10,11}, Russell E. Ryan¹, Daniel Lam³², Irene Sendra-Server³³, Sune Toft^{9,24}, Lorenzo Lovisari¹⁴, and Yuanyuan Su³⁴

¹ Space Telescope Science Institute, 3700 San Martin Drive, Baltimore, MD 21218, USA; DCoe@STScI.edu

² Department of Physics, University of California, Davis, CA 95616, USA

³ Department of Astronomy, University of Michigan, 1085 South University Avenue, Ann Arbor, MI 48109, USA

⁴ Physics Department, Ben-Gurion University of the Negev, P.O. Box 653, Beer-Sheva 84105, Israel

⁵ Astronomy Department and Institute for Astrophysical Research, Boston University, 725 Commonwealth Avenue, Boston, MA 02215, USA

⁶ Department of Physics and Astronomy, University of California, Riverside, CA 92521, USA

⁷ Department of Astronomy, Steward Observatory, University of Arizona, 933 North Cherry Avenue, Tucson, AZ 85721, USA

⁸ Department of Astronomy, University of Geneva, Chemin des Maillettes 51, 1290 Versoix, Switzerland

⁹ Cosmic Dawn Center (DAWN), Copenhagen, Denmark

¹⁰ School of Physics, University of Melbourne, VIC 3010, Australia

¹¹ ARC Centre of Excellence for All Sky Astrophysics in 3 Dimensions (ASTRO 3D), VIC 2010, Australia

¹² Lawrence Livermore National Laboratory, P.O. Box 808 L-210, Livermore, CA 94551, USA

¹³ Department of Physics and Astronomy, University of South Carolina, 712 Main Street, Columbia, SC 29208, USA

¹⁴ Harvard-Smithsonian Center for Astrophysics, 60 Garden Street, Cambridge, MA 02138, USA

¹⁵ Academia Sinica Institute of Astronomy and Astrophysics (ASIAA), No. 1, Section 4, Roosevelt Road, Taipei 10617, Taiwan

¹⁶ INAF-Osservatorio Astronomico di Padova, Vicolo Dell'osservatorio 5, I-35122 Padova, Italy

¹⁷ Department of Astrophysics, American Museum of Natural History, Central Park West and 79th Street, New York, NY 10024-5192, USA

¹⁸ Department of Physics and Astronomy, Rutgers, The State University of New Jersey, 136 Frelinghuysen Road, Piscataway, NJ 08854, USA

¹⁹ Department of Astronomy, University of Washington, Box 351580, U.W., Seattle, WA 98195-1580, USA

²⁰ Universidade de São Paulo, Instituto de Astronomia, Geofísica e Ciências Atmosféricas, Rua do Matão 1226, São Paulo, Brazil

²¹ Instituto de Astrofísica de Andalucía (IAA-CSIC), E-18080 Granada, Spain

²² INAF—Osservatorio Astronomico di Trieste, Via Tiepolo 11, I-34131 Trieste, Italy

²³ DARK, Niels Bohr Institute, University of Copenhagen, Lyngbyvej 2, DK-2100 Copenhagen, Denmark

²⁴ Niels Bohr Institute, University of Copenhagen, Lyngbyvej 2, DK-2100, Copenhagen, Denmark

²⁵ Institute for Cosmic Ray Research, The University of Tokyo, 5-1-5 Kashiwanoha, Kashiwa, Chiba 277-8582, Japan

²⁶ Department of Astronomy, Graduate School of Science, The University of Tokyo, 7-3-1 Hongo, Bunkyo, Tokyo, 113-0033, Japan

²⁷ Kavli Institute for the Physics and Mathematics of the Universe (Kavli IPMU, WPI), University of Tokyo, Kashiwa, Chiba 277-8583, Japan

²⁸ Research Center for the Early Universe, The University of Tokyo, 7-3-1 Hongo, Bunkyo-ku, Tokyo 113-0033, Japan

²⁹ Department of Physics, The University of Tokyo, 7-3-1 Hongo, Bunkyo-ku, Tokyo 113-0033, Japan

³⁰ Department of Physics and Astronomy, Johns Hopkins University, 3400 North Charles Street, Baltimore, MD 21218, USA

³¹ Department of Astronomy, University of Michigan, 1085 South University Drive, Ann Arbor, MI 48109, USA

³² Leiden Observatory, Leiden University, NL-2300 RA Leiden, The Netherlands

³³ Department of Theoretical Physics, University of the Basque Country UPV/EHU, E-48080 Bilbao, Spain

³⁴ Department of Physics and Astronomy, University of Kentucky, 505 Rose Street, Lexington, KY 40506, USA

Received 2019 March 5; revised 2019 August 6; accepted 2019 September 2; published 2019 October 14

Abstract

Large surveys of galaxy clusters with the *Hubble Space Telescope* (*HST*) and *Spitzer*, including the Cluster Lensing And Supernova survey with Hubble and the Frontier Fields, have demonstrated the power of strong gravitational lensing to efficiently deliver large samples of high-redshift galaxies. We extend this strategy through a wider, shallower survey named RELICS, the Reionization Lensing Cluster Survey, described here. Our 188-orbit Hubble Treasury Program observed 41 clusters at $0.182 \leq z \leq 0.972$ with Advanced Camera for Surveys (ACS) and WFC3/IR imaging spanning $0.4\text{--}1.7\ \mu\text{m}$. We selected 21 of the most massive clusters known based on *Planck* PSZ2 estimates and 20 additional clusters based on observed or inferred lensing strength. RELICS observed 46 WFC3/IR pointings ($\sim 200\text{ arcmin}^2$) each with two orbits divided among four filters (F105W, F125W, F140W, and F160W) and ACS imaging as needed to achieve single-orbit depth in each of three filters (F435W, F606W, and F814W). As previously reported by Salmon et al., we discovered over 300 $z \sim 6\text{--}10$ candidates, including the brightest $z \sim 6$ candidates known, and the most distant spatially resolved lensed arc known at $z \sim 10$. *Spitzer* IRAC imaging (945 hr awarded, plus 100 archival, spanning $3.0\text{--}5.0\ \mu\text{m}$) has crucially enabled us to distinguish $z \sim 10$ candidates from $z \sim 2$ interlopers. For each cluster, two *HST* observing epochs were staggered by about a month, enabling us to discover 11 supernovae, including 3 lensed supernovae, which we followed up with

³⁵ NSF Astronomy and Astrophysics Postdoctoral Fellow.

20 orbits from our program. Reduced *HST* images, catalogs, and lens models are available on MAST, and reduced *Spitzer* images are available on IRSA.

Key words: dark ages, reionization, first stars – dark matter – galaxies: clusters: general – galaxies: high-redshift – gravitational lensing: strong – supernovae: general

1. Introduction

Gravitational lensing magnification by massive galaxy clusters has a long history of helping astronomers discover the most distant galaxies known with the *Hubble Space Telescope* (*HST*) and *Spitzer* (see Kneib & Natarajan 2011 Section 5.8 for a review). Twenty years ago, a $z = 4.92$ galaxy lensed by the cluster MS 1358+62 was the most distant known (Franx et al. 1997). Ten years ago, that record belonged to A1689-zD1 at $z \sim 7.5$ (Bradley et al. 2008; Watson et al. 2015). More recently, the Cluster Lensing And Supernova survey with Hubble (CLASH; Postman et al. 2012) yielded the triply imaged $z \sim 10.8$ candidate MACS0647-JD (Coe et al. 2013; Pirzkal et al. 2015; Chan et al. 2017). This redshift has been surpassed only by the grism measurement of $z = 11.1$ (Oesch et al. 2016) for GN-z11 discovered by Oesch et al. 2014 in blank-field imaging by the CANDELS program (Grogin et al. 2011; Koekemoer et al. 2011). Both $z \sim 11$ galaxies are similarly bright at $1.6 \mu\text{m}$ (F160W AB mag 25.9), making them excellent targets for follow-up study with the *James Webb Space Telescope* (*JWST*).

For a given observing strategy, lensed fields generally yield significantly more high-redshift galaxies than blank fields, especially at the highest redshifts and in relatively shallow imaging (e.g., Coe et al. 2015). Lensing does sacrifice high-redshift search volume owing to the magnification and the foreground cluster light. But lensing more than compensates for the lost volume by magnifying many more faint galaxies into view whenever luminosity function number counts are steeper than $\phi \propto L^{-2}$ (Broadhurst et al. 1995). This is especially true brightward of L^* , for example, AB mag ~ 28 at $z \sim 8$ (Bradley et al. 2012; Finkelstein 2016).

CLASH demonstrated this lensing advantage, yielding significantly more galaxies at $z \sim 6$ –8 than blank-field surveys (Bradley et al. 2014). CLASH obtained 20-orbit *HST* imaging for each of 25 clusters in 16 filters, including F160W observed to AB mag 27.5 (5σ depth; Postman et al. 2012; Molino et al. 2017). The first 18 clusters yielded 262 candidates at $z \sim 6$ –8 (Bradley et al. 2014), plus a few at $z \sim 9$ –11 (Zheng et al. 2012; Coe et al. 2013; Bouwens et al. 2014).

The Frontier Fields (Lotz et al. 2017) obtained deeper 140-orbit *HST* imaging for each of six clusters and six blank parallel fields in seven filters, including F160W observed to AB mag 28.7. At these depths, $\phi \propto L^{-2}$ for high-redshift galaxies (the luminosity function faint-end slope $\alpha \sim -2$ roughly at $z \sim 6$ –8), so the lensed and blank-field high- z counts were predicted to be similar (Coe et al. 2015). Indeed, the Frontier Fields yielded similar total numbers of lensed and blank-field high-redshift galaxies, altogether 453 at $z \sim 6$ –9 from one analysis (Kawamata et al. 2018), plus a few $z \sim 10$ candidates (Zitrin et al. 2014; Infante et al. 2015; McLeod et al. 2016; Oesch et al. 2018). Due to their magnifications, the lensed galaxies are intrinsically fainter than the blank-field galaxies. By combining deep *HST* imaging with the power of gravitational lensing, the Frontier Fields revealed the faintest galaxies yet known, including some of those likely responsible for reionization at $z \sim 6$ (Livermore et al. 2017; Atek et al. 2018).

While CLASH and the Frontier Fields yielded many high-redshift candidates, neither survey was optimized to deliver high-redshift candidates observed brightly enough for detailed follow-up study with current and future observatories. Detailed studies are required to determine galaxies’ ages, stellar masses, compositions, and ionizing strengths (see Stark 2016 for a review). This knowledge can further inform how early galaxies enriched and reionized the universe (see Dayal & Ferrara 2018 for a review). It is imperative to use existing facilities to discover the best targets for study, ideally before *JWST* Cycle 1. Gravitational lensing offers the most efficient route to do this. The *Planck* all-sky survey delivered the PSZ2 catalog of >1000 massive galaxy clusters (Planck Collaboration et al. 2016a) detected via their Sunyaev–Zel’dovich (SZ) effect (Sunyaev & Zeldovich 1970) on the cosmic microwave background (CMB). By searching the PSZ2 catalog, we found that many massive clusters (including presumably excellent lenses) lacked the combination of *HST* Advanced Camera for Surveys (ACS) and Wide Field Camera 3 infrared (WFC3/IR) imaging required to discover high-redshift candidates at $z > 6$.

RELICS embarked on an efficient survey with *HST* and *Spitzer* to discover the best and brightest high-redshift galaxies (Coe 2018). RELICS obtained five-orbit *HST* imaging of 41 clusters in seven filters (the same filters used by the Frontier Fields), including F160W to AB mag 26.5. Our relatively shallow imaging covered more area than CLASH or the Frontier Fields, yielding high-redshift candidates that are brighter, either intrinsically and/or due to lensing magnification. See Table 1 for a summary comparison of CLASH, the Frontier Fields, and RELICS. More recently, a new *HST* program, BUFFALO (PIs Steinhardt & Jauzac; GO 15117), has begun, extending the Frontier Fields to the wider area covered by deep *Spitzer* imaging.

Also notable and inspiring for this project are the *HST* Snapshot programs observing galaxy clusters discovered by the MASSive Cluster Survey (MACS; Ebeling et al. 2001). Shallower *HST* imaging (~ 1 orbit per cluster) has been obtained for 86 clusters to date (Repp & Ebeling 2018). For 29 of these clusters, four-band imaging, including F140W to AB mag 26.6, was completed, yielding 20 candidates at $z \sim 7$ –9 (Repp et al. 2016). Nine MACS clusters are included in RELICS. Prior to RELICS, they had archival *HST* ACS and/or WFPC2 imaging, but not WFC3/IR or NICMOS.

Meanwhile, large *Spitzer* programs such as SURFS UP (Bradač et al. 2014; Ryan et al. 2014; Huang et al. 2016) and the Frontier Fields have also surveyed many galaxy clusters, helping to identify high-redshift galaxies and study their properties (e.g., Hoag et al. 2019). The Grism Lens-Amplified Survey from Space (Treu et al. 2015) delivered spectroscopic properties and high-redshift confirmations (e.g., Schmidt et al. 2016, 2017). The high-redshift searches in lensing programs complement searches in blank-field surveys such as the UDF, CANDELS, and BoRG, constraining luminosity functions from $z \sim 4$ to 10 (Bouwens et al. 2015; Finkelstein 2016; Morishita et al. 2018; Oesch et al. 2018).

Table 1
Recent Large *HST* Cluster Lensing Surveys

	CLASH	Frontier Fields	RELICS
Clusters	25	6	41
<i>HST</i> orbits per cluster	20 ^a	140	5 ^a
Total <i>HST</i> orbits	524	840	188
Supernova orbits ^b	50	0	20
<i>HST</i> filters	16	7	7
Depth in F160W ^c	27.5	28.7	26.5
<i>HST</i> Cycle numbers	18–20	21–23	23
<i>HST</i> begin	Nov 10	Oct 13	Oct 15
<i>HST</i> end	Jul 13	Sept 16	Apr 17

Notes.

^a Depth including archival *HST* imaging.

^b *HST* orbits allocated specifically for supernova follow-up.

^c AB mag 5σ depth for point sources.

Below we discuss the RELICS science drivers (Section 2); galaxy cluster targets (Section 3); observations with *HST*, *Spitzer*, and other observatories (Section 4); the image reductions and catalogs (Section 5); results to date (Section 6); and a summary (Section 7).

We use the AB magnitude system, $m_{AB} = 31.4 - 2.5 \log(f_\nu/nJy)$ (Oke 1974; Oke & Gunn 1983). Where needed, we assume a flat concordance Λ CDM cosmology with $h = 0.7$, $\Omega_m = 0.3$, and $\Omega_\Lambda = 0.7$, where $H_0 = 100 h \text{ km s}^{-1} \text{ Mpc}^{-1}$. Galaxy cluster masses are given as M_{500} , the mass enclosed within r_{500} , within which the average density is 500 times the critical density of the universe at that redshift (e.g., Coe 2010). These masses M_{500} are less than the total virial cluster masses measured at larger radii.

2. Science

RELICS was primarily designed and optimized to search for brightly lensed high-redshift galaxies in the epoch of reionization. Ancillary science enabled by RELICS includes supernova (SN) searches, cluster mass measurements, and limits on the dark matter particle cross section. We discuss each of these science goals in turn.

2.1. High-redshift Galaxies

HST's WFC3 has revealed ~ 2000 $z \sim 6$ –11 candidates from the universe's first billion years, but only a small fraction have been bright enough ($H < 25.5$) for detailed follow-up study and spectroscopic confirmation (e.g., Bouwens et al. 2015; Salmon et al. 2017). RELICS was designed primarily to deliver (1) brightly observed high-redshift candidates, amenable to more detailed studies; and (2) a large sample of high-redshift candidates to improve luminosity function constraints. This combination is required to improve our understanding of galaxies and reionization in the first billion years.

2.1.1. Spectroscopic Studies of Brightly Observed High-redshift Candidates

Spectroscopic redshift confirmations based on $\text{Ly}\alpha$ detections have proven increasingly difficult beyond $z > 6$ (Stark et al. 2010; Bradač et al. 2012; Schenker et al. 2014; Schmidt et al. 2016; Hoag et al. 2019; Mason et al. 2019), likely due primarily to absorption by patchy neutral hydrogen before reionization was complete (Treu et al. 2013; Tilvi et al. 2014;

Mason et al. 2018). A higher success rate was achieved with four luminous $z \sim 7$ –9 galaxies inferred to have significant $[\text{O III}] + \text{H}\beta$ equivalent width (EW) based on *Spitzer* photometry (Roberts-Borsani et al. 2016). All four yielded $\text{Ly}\alpha$ detections as distant as $z = 8.68$ (Oesch et al. 2015; Zitrin et al. 2015b; Stark et al. 2017). This suggests that luminous galaxies with high ionization parameters carve out ionized gas bubbles allowing $\text{Ly}\alpha$ to stream free (Stark et al. 2017).

Alternatives to $\text{Ly}\alpha$ redshift confirmations include fainter, slightly redder UV metal lines such as $\text{N V } \lambda 1243$, $\text{C IV } \lambda 1549$, $\text{He II } \lambda 1640$, $\text{O III } \lambda 1663$, and $\text{C III } \lambda 1908$ (Stark et al. 2014) and submillimeter lines such as $[\text{C II}] 158 \mu\text{m}$ and $[\text{O III}] 88 \mu\text{m}$ (Inoue et al. 2014). Studying these lines also yields more information about the physical properties of the galaxies, including their ionizing strength.

The UV metal line C III has been detected in several $z > 6$ galaxies as distant as $z = 7.73$ (Stark et al. 2015, 2017; Laporte et al. 2017a; Mainali et al. 2018). At $z \sim 2$, Rigby et al. (2015) found that lower-metallicity galaxies exhibit stronger C III , likely explaining why C III appears far more often at $z \sim 6$ than at lower redshifts (see also Senchyna et al. 2017; Du et al. 2017; Le Fèvre et al. 2019). C III detections may be powered by low-metallicity massive stars (Stark et al. 2015, 2017) or may require active galactic nuclei (AGNs; Nakajima et al. 2018). Still lower-metallicity stars ($< 0.05 Z_\odot$) produce higher ionization potentials yielding C IV . All three known $z > 6$ C IV detections are lensed (Stark et al. 2015; Hoag et al. 2017; Mainali et al. 2017) and thus less massive and presumably lower metallicity than average $z > 6$ galaxies from current surveys.

Larger samples of UV metal line observations including RELICS galaxies will enable us to quantify the prevalence of these intense ionizing sources in the reionization epoch, both directly and by extrapolating to larger samples with similar observed properties (luminosity, rest-frame UV slope β , and $\text{Ly}\alpha$). The observed EWs will also be very informative to future *JWST* surveys planning to observe these spectral features.

A new window for studying high-redshift galaxies has been opened by the Atacama Large Millimeter/submillimeter Array (ALMA) in the south and the Plateau de Bure interferometer (PdBI) in the north, later upgraded and renamed the Northern Extended Millimeter Array (NOEMA). These telescopes (primarily ALMA) have detected high-redshift galaxies by their infrared continuum dust emission (Capak et al. 2015), as well as spectral lines $[\text{C II}] 158 \mu\text{m}$ and $[\text{O III}] 88 \mu\text{m}$, which trace star formation (De Looze et al. 2014). Continuum observations show that $z \sim 5$ –6 galaxies have at least an order of magnitude less dust than local starbursts with similar rest-frame UV colors (Capak et al. 2015). Dust is often not detected at these redshifts, but at least a few galaxies have been found to be dusty and thus evolved as early as $z = 7.15$ (Hashimoto et al. 2019), $z = 7.5$ (Watson et al. 2015), $z = 8.312$ (Tamura et al. 2019), and $z = 8.38$ (Laporte et al. 2017a).

$[\text{C II}] 158 \mu\text{m}$ is one of the brightest lines in local galaxies (Malhotra et al. 1997; Brauher et al. 2008) and the strongest observed interstellar medium cooling line in $z \sim 1$ –2 galaxies (Stacey et al. 2010). To date, $[\text{C II}]$ has been detected in 22 galaxies between $5.1533 \leq z \leq 7.1453$ (Carniani et al. 2018 and references therein; Hashimoto et al. 2019), including two spatially resolved galaxies at $z = 6.81$ and 6.85 displaying disk-like rotation (Smit et al. 2018).

Table 2
RELICS Clusters

Index	Cluster ^a	R.A. ^b (J2000)	Decl. ^b (J2000)	Redshift	Planck Mass M_{500}		$E(B - V)$
					Rank ^c	($10^{14} M_{\odot}$)	
1	A2163 NE	16:15:48.3	−06:07:36.7	0.203	1	$16.12^{+0.30}_{-0.29}$	0.2972
	A2163 SW	16:15:42.6	−06:09:22.1				
2	PLCK G287.0+32.9	11:50:50.8	−28:04:52.2	0.390 ^d	2	$14.69^{+0.39}_{-0.42}$	0.0813
3	MACS J0417.5-1154	04:17:33.7	−11:54:22.6	0.443	4	$12.25^{+0.53}_{-0.55}$	0.0320
4	A697	08:42:58.9	+36:21:51.1	0.282	10	$11.00^{+0.37}_{-0.37}$	0.0333
5	RXS J060313.4+4212 N	06:03:12.2	+42:15:24.7	0.228	11	$10.76^{+0.45}_{-0.43}$	0.1933
	RXS J060313.4+4212 S	06:03:25.6	+42:09:53.6				
6	MACS J0308.9+2645	03:08:55.7	+26:45:36.8	0.356	12	$10.76^{+0.63}_{-0.65}$	0.1776
7	ACT-CL J0102-49151 NW	01:02:53.1	−49:14:52.8	0.870	13	$10.75^{+0.48}_{-0.47}$	0.0086
	ACT-CL J0102-49151 SE	01:03:00.0	−49:16:22.2				
8	RXC J0600.1-2007	06:00:09.8	−20:08:08.9	0.460	14	$10.73^{+0.51}_{-0.54}$	0.0433
9	PSZ2 G209.79+10.23	07:22:23.0	+07:24:30.0	0.677	15	$10.73^{+0.63}_{-0.66}$	0.0375
10	PLCK G171.9-40.7	03:12:56.9	+08:22:19.2	0.270	16	$10.71^{+0.49}_{-0.50}$	0.4477
11	RXC J2211.7-0350	22:11:45.9	−03:49:44.7	0.397	17	$10.50^{+0.50}_{-0.49}$	0.0832
12	PLCK G004.5-19.5	19:17:04.5	−33:31:28.5	0.519 ^e	19	$10.36^{+0.68}_{-0.72}$	0.0790
13	PLCK G308.3-20.2	15:18:49.9	−81:30:33.6	0.480	20	$10.32^{+0.57}_{-0.58}$	0.2348
14	RXC J0018.5+1626	00:18:32.6	+16:26:08.4	0.546	24	$9.79^{+0.53}_{-0.53}$	0.0501
15	SPT-CL J0254-5857	02:54:16.0	−58:57:11.0	0.438	26	$9.69^{+0.37}_{-0.38}$	0.0183
16	PSZ2 G138.61-10.84	02:27:06.6	+49:00:29.9	0.702	27	$9.48^{+0.67}_{-0.53}$	0.1830
17	RXC J0142.9+4438	01:42:55.2	+44:38:04.3	0.341	28	$9.02^{+0.60}_{-0.64}$	0.0783
18	A1300	11:31:54.1	−19:55:23.4	0.308	30	$8.97^{+0.46}_{-0.45}$	0.0440
19	WHL J013719.8-082841	01:37:25.0	−08:27:25.0	0.566	31	$8.93^{+0.65}_{-0.70}$	0.0286
20	RXC J1514.9-1523	15:15:00.7	−15:22:46.7	0.223	33	$8.86^{+0.41}_{-0.46}$	0.0869
21	A665	08:30:57.4	+65:50:31.0	0.182	34	$8.86^{+0.32}_{-0.32}$	0.0400
22	MACS J0553.4-3342	05:53:23.1	−33:42:29.9	0.430	36	$8.77^{+0.44}_{-0.46}$	0.0357
23	SMACS J0723.3-7327	07:23:19.5	−73:27:15.6	0.390	43	$8.39^{+0.33}_{-0.34}$	0.1893
24	RXC J0949.8+1707	09:49:50.9	+17:07:15.3	0.383	48	$8.24^{+0.46}_{-0.46}$	0.0255
25	A1758a NW	13:32:39.0	+50:33:41.8	0.280	50	$8.22^{+0.27}_{-0.28}$	0.0122
	A1758a SE	13:32:53.4	+50:31:31.0				
26	A1763	13:35:18.9	+40:59:57.2	0.228	51	$8.13^{+0.26}_{-0.27}$	0.0073
27	A2813	00:43:25.1	−20:37:14.8	0.292	52	$8.13^{+0.37}_{-0.38}$	0.0178
28	A520 NE	04:54:19.0	+02:56:49.0	0.203	65	$7.80^{+0.40}_{-0.41}$	0.0402
	A520 SW	04:54:04.2	+02:53:41.9				
29	RXC J0032.1+1808	00:32:11.0	+18:07:49.0	0.396	85	$7.61^{+0.57}_{-0.63}$	0.1052
30	RXC J0232.2-4420	02:32:18.1	−44:20:44.9	0.284	91	$7.54^{+0.33}_{-0.32}$	0.0165
31	A3192 ^f	03:58:53.1	−29:55:44.8	0.425	114	$7.20^{+0.52}_{-0.50}$	0.0071
32	MACS J0159.8-0849	01:59:49.4	−08:50:00.0	0.405	115	$7.20^{+0.61}_{-0.68}$	0.0207
33	MACS J0035.4-2015	00:35:27.0	−20:15:40.3	0.352	133	$7.01^{+0.45}_{-0.50}$	0.0187
34	RXC J0911.1+1746	09:11:11.4	+17:46:33.5	0.505	136	$6.99^{+0.73}_{-0.79}$	0.0359
35	AS295	02:45:31.4	−53:02:24.9	0.300	156	$6.78^{+0.37}_{-0.36}$	0.0445
36	SPT-CL J0615-5746	06:15:54.2	−57:46:57.9	0.972	157	$6.77^{+0.49}_{-0.54}$	0.0362
37	MACS J0257.1-2325	02:57:10.2	−23:26:11.8	0.505	227	$6.22^{+0.70}_{-0.74}$	0.0251
38	A2537	23:08:22.2	−02:11:32.4	0.297	376	$5.52^{+0.51}_{-0.51}$	0.0798
39	MS 1008.1-1224	10:10:33.6	−12:39:43.0	0.306	504	$4.94^{+0.57}_{-0.60}$	0.0601
40	MACS J0025.4-1222	00:25:30.3	−12:22:48.1	0.586	0.0239
41	CL J0152.7-1357	01:52:42.9	−13:57:31.0	0.833	0.0126

Notes.^a Cluster name and portion (e.g., NE) if observed by RELICS with two WFC3/IR pointings.^b Coordinates of *HST* WFC3/IR pointings.^c Mass rank among all 1094 clusters in the PSZ2 catalog.^d Redshift updated in Zitrin et al. (2017); previously $z = 0.38$.^e Redshift updated in Albert et al. (2017); previously $z = 0.54$.^f Observations of MACS J0358.8-2955 ($z = 0.428$) include contributions from A3192 ($z = 0.168$).

At higher redshifts, Inoue et al. (2014) predicted that [O III] 88 μm would yield more detections. While [C II] is associated with neutral H I gas in photodissociation regions (PDRs), [O III]

is associated with ionized H II gas, more prevalent in higher-redshift, lower-metallicity galaxies with higher ionization states (Harikane et al. 2018). As predicted, ALMA's highest-redshift

Table 3
RELICS Cluster Names

Index	Cluster	Alternate Name	Abbreviation	Notes
1	A2163		abell2163	
2	PLCK G287.0+32.9		plckg287+32	
3	MACS J0417.5-1154		macs0417-11	(a)
4	A697		abell697	
5	RXS J060313.4+4212	“Toothbrush”	rxs0603+42	
6	MACS J0308.9+2645		macs0308+26	
7	ACT-CL J0102-49151	“El Gordo”	act0102-49	(b)
8	RXC J0600.1-2007	MACS J0600.1-2007		
9	PSZ2 G209.79+10.23		plckg209+10	
10	PLCK G171.9-40.7		plckg171-40	
11	RXC J2211.7-0350	MACS J2211.7-0350	rxs2211-03	
12	PLCK G004.5-19.5		plckg004-19	
13	PLCK G308.3-20.2	SMACS J1519.1-8130	plckg308-20	
14	RXC J0018.5+1626	MS0015.9+1609 MACS J0018.5+1626	rxs0018+16	
15	SPT-CL J0254-5857		spt0254-58	
16	PSZ2 G138.61-10.84		plckg138-10	(c)
17	RXC J0142.9+4438	CIZA J0142.9+4438	rxs0142+44	
18	A1300		abell1300	
19	WHL J013719.8-082841	WHL J24.3324-8.477	whl0137-08	(d)
20	RXC J1514.9-1523		rxs1514-15	
21	A665		abell665	
22	MACS J0553.4-3342		macs0553-33	
23	SMACS J0723.3-7327		smacs0723-73	
24	RXC J0949.8+1707		rxs0949+17	(e)
25	A1758a		abell1758	
26	A1763		abell1763	
27	A2813		abell2813	
28	A520	“Train Wreck”	abell520	
29	RXC J0032.1+1808		rxs0032+18	
30	RXC J0232.2-4420	“RBS-0325”	rxs0232-44	
31	A3192	MACS J0358.8-2955	abell3192	(f)
32	MACS J0159.8-0849		macs0159-08	(g)
33	MACS J0035.4-2015		macs0035-20	
34	RXC J0911.1+1746	MACS J0911.1+1746	rxs0911+17	
35	AS295	ACT-CL J0245-5302 SPT-CL J0245-5302	abells295	
36	SPT-CL J0615-5746		spt0615-57	
37	MACS J0257.1-2325		macs0257-23	(h)
38	A2537		abell2537	(h)
39	MS 1008.1-1224		ms1008-12	
40	MACS J0025.4-1222	“Baby Bullet”	macs0025-12	
41	CL J0152.7-1357		cl0152-13	

Notes.

^a *JWST* GTO target (CANUCS; PI Willott).

^b *JWST* GTO target (PI Windhorst).

^c Optical counterpart is 4¹/₅ from PSZ1 coordinates (2:27:06, +49:05:10) from Planck Collaboration et al. (2016d).

^d Discovered by Wen et al. (2012) based on photometric redshifts in SDSS-III. Renamed in the PSZ2 catalog with coordinates given in decimal degrees (Alternate Name above).

^e Wong et al. (2013) #7: seventh most powerful lensing line of sight expected based on LRGs identified in SDSS.

^f *HST* observations centered on MACS0358 ($z = 0.428$); includes some contribution from A3192 ($z = 0.168$). See Hamilton-Morris et al. (2012) and Hsu et al. (2013).

^g Wong et al. (2013) #59.

^h Frontier Fields contender (ultimately not selected).

spectroscopic confirmations have come from [O III], and the six $z > 6$ galaxies targeted to date have all yielded [O III] detections at $z = 6.900$ (Marrone et al. 2018), $z = 7.107$ (Carniani et al. 2017), $z = 7.212$ (Inoue et al. 2016), $z = 8.312$ (Tamura et al. 2019), $z = 8.382$ (Laporte et al. 2017b), and $z = 9.11$ (Hashimoto et al. 2018). The two highest-redshift detections are lensed galaxies.

Based on this previous work, we expect RELICS to deliver ALMA confirmations and science at $z \sim 6$ –10 (see Section 6.1).

2.1.2. Luminosity Functions of Galaxies at the Epoch of Reionization

Improving constraints on the $z \sim 9$ luminosity function (and the evolution from $z \sim 10$ to 6) is another primary science goal of RELICS. This is required to determine the numbers of faint galaxies available to reionize the universe.

Planck constrained the reionization history by measuring the column density of free electrons to the CMB, or the Thomson scattering optical depth $\tau = 0.058 \pm 0.012$ (Planck Collaboration et al. 2018a). This value, lower than previous estimates,

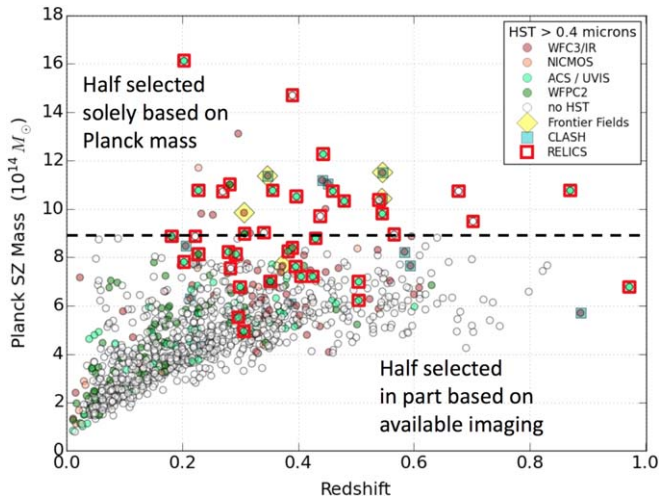


Figure 1. RELICS clusters marked as red squares on a plot of mass vs. redshift for the 1094 clusters in the Planck PSZ2 catalog. Each cluster is plotted as a circle color-coded according to existing *HST* imaging prior to RELICS, prioritizing WFC3/IR (red) followed by NICMOS (salmon), ACS and/or UVIS (aqua), and finally WFPC2 (green). Clusters without *HST* imaging prior to RELICS are colored white. Frontier Fields and CLASH clusters are plotted as filled yellow diamonds and blue squares, respectively. A dashed line at $8.7 \times 10^{14} M_{\odot}$ separates the 21 clusters selected solely by mass from the other 20 selected based on various criteria, including existing imaging revealing lensing strength. Note that two RELICS clusters are not plotted here, as they were not included in the Planck PSZ2 catalog.

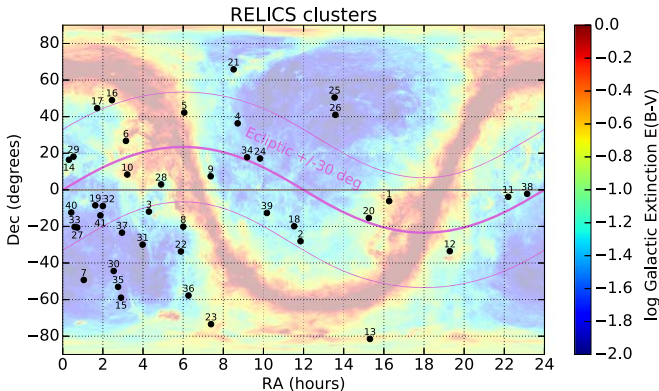


Figure 2. Distribution on the sky of the 41 RELICS clusters relative to the Galactic and ecliptic planes. The background is color-coded to show the Galactic extinction map from Schlegel et al. (1998). Numbers correspond to ordered Planck mass as given in Table 2.

implies a later reionization halfway complete by $z \sim 8$, before fully completing by $z \sim 6$. It also means that reionization can be achieved by galaxies producing less Lyman continuum (LyC) flux and with lower escape fractions f_{esc} . Direct measurements of these f_{esc} values have been obtained recently for ~ 40 galaxies with detected LyC leakage, including half extending from the local universe (e.g., Leitherer et al. 2016; Puschnig et al. 2017) to $z \sim 0.3$ (e.g., Izotov et al. 2018), with the other half at $z \sim 2-4$ (e.g., Shapley et al. 2016; Rivera-Thorsen et al. 2017; Vanzella et al. 2018). Assuming that these measurements hold at higher redshifts, and given high-redshift luminosity functions, low-mass galaxies could have produced most of the flux required to reionize the universe (e.g., Robertson et al. 2015; Madau 2017; Ishigaki et al. 2018; Mason et al. 2018; Finkelstein et al. 2019). There may also

have been significant contributions from low-luminosity AGN jets at $z \gtrsim 6$ (Bosch-Ramon 2018).

At the highest redshifts ($z \sim 9-12$), *HST* and *Spitzer* imaging programs have yielded fewer candidates than expected. This has left luminosity functions highly uncertain at these redshifts, while also hinting at accelerated evolution in the first 600 Myr (Bouwens et al. 2012; Oesch et al. 2018). Luminosity functions are fairly well constrained at $z \sim 4-8$ (Bouwens et al. 2015; Finkelstein 2016; Kawamata et al. 2018). Only recently were constraints placed on all three parameters (ϕ^* , M^* , α) of the $z \sim 9$ luminosity function (Morishita et al. 2018); these results are consistent with either accelerated or smoother (nonaccelerated) evolution at $z > 8$. Higher-precision measurements, especially with greater leverage at higher redshifts, are required to better constrain this early evolution rate.

2.2. Strong-lens Modeling

Robust strong-lens modeling is required to estimate magnifications of our lensed galaxies and the survey volume. The mass in galaxy cluster cores responsible for the lensing is predominantly dark matter. We must infer the distribution of this dark matter based on observed strong lensing that produces multiple images of more distant galaxies. We often add the assumption that luminous galaxy cluster members are good tracers of their dark matter halos.

High-quality lens modeling generally requires multiband high-resolution *HST* imaging to reliably identify multiple images of strongly lensed galaxies based on their colors and morphologies. Spectroscopic redshifts are also crucial. Magnification accuracies improve with greater numbers of strongly lensed images with spectroscopic redshifts (Johnson & Sharon 2016). Recent tests with simulated cluster lensing find that the best lens models accurately yield magnification estimates of 3 (10) with precisions of 15% (30%), with uncertainty increasing with magnification (Meneghetti et al. 2017; see also Zitrin et al. 2015a). Such precision is encouraging, as the vast majority (over 80%) of lensed high-redshift galaxies observed are magnified by factors of 10 or less (Coe et al. 2015).

Magnification uncertainties directly impact measurements of some physical properties such as luminosity, star formation rate, stellar mass, and size. However, since lensing is achromatic, other properties derived from galaxy colors are not affected by magnification; these include redshift, age, metallicity, extinction, and rest-frame UV slope. Magnifications do affect luminosity functions, but the uncertainties are mitigated by averaging over many galaxies. The resulting uncertainties on the total survey volume are subdominant compared to the current small number statistics at high redshifts (Coe et al. 2015).

In the case of a multiply imaged high-redshift candidate, lens modeling can yield geometric support, distinguishing between low- and high-redshift solutions based on the separation between the observed images (e.g., Coe et al. 2013; Zitrin et al. 2014; Chan et al. 2017). Lens modeling is required to study delensed (source plane) properties, including ~ 100 pc structures resolved in highly elongated arcs (e.g., Sharon et al. 2012; Johnson et al. 2017). Lens modeling is also required to constrain luminosity functions in lensed fields (e.g., Livermore et al. 2017).

RELICS lens modeling is yielding the overall lensing strength for each cluster. While we expect all RELICS clusters to be excellent lenses, our analyses will reveal which are truly among the strongest and best to use for efficient discoveries of

Table 4
Archival *HST* ACS and WFC3/UVIS Imaging of RELICS Clusters

Cluster Index	Abbreviated Name ^a	F390W (s)	F435W (s)	F475W (s)	F555W (s)	F606W (s)	F625W (s)	F775W (s)	F814W (s)	F850LP (s)
1	abell2163		4664 ^b			4667 ^b			9192 ^b	
2	plckg287+32			2160		2320			4680	
3	macs0417-11					7152 ^c			1910	
4	abell697									
5	rxs0603+42	5294 ^{b,c}				5068 ^{b,c}			10194 ^b	
6	macs0308+26					1200			1440	
7	act0102-49					7680 ^b	4688 ^b	5024 ^b	1916	5032 ^b
8	rxs0600-20								1440	
9	plckg209+10									
10	plckg171-40									
11	rxs2211-03					1200				
12	plckg004-19									
13	plckg308-20					1200				
14	rxs0018+16				4500	17920 ^b		4623	4560	2540
15	spt0254-58									
16	plckg138-10									
17	rxs0142+44									
18	abell1300									
19	whl0137-08									
20	rxs1514-15									
21	abell665						2680			
22	macs0553-33		4452			2092			4572	
23	smacs0723-73					1200			1440	
24	rxs0949+17					1200			1440	
25	abell1758		5072 ^b			5088 ^b			10000 ^b	
26	abell1763									
27	abell2813					1200				
28	abell520		9296 ^b			9328 ^b			18320 ^b	
29	rxs0032+18					1200			1440	
30	rxs0232-44									
31	abell3192		4500			3320			4620	
32	macs0159-08					1200				
33	macs0035-20					1200			1440	
34	rxs0911+17				4470				8825	
35	abells295		1920			1936			3944	
36	spt0615-57					8880 ^b			12720 ^d	
37	macs0257-23				4500				8858	
38	abell2537					2080				
39	ms1008-12					17856 ^b		2440		2560
40	macs0025-12				4140				4200	
41	cl0152-13						19000 ^b	23452 ^d		19000 ^b

Notes.

^a Abbreviated names provided here are used elsewhere in the text and in data product filenames.

^b Multiple pointings with minimal or no overlap are given in superscript brackets. Total exposure times listed should be divided by the numbers [2] or [4] to give the depth at each position.

^c WFC3/UVIS observations. (All other archival observations listed are ACS.)

^d 2 × 2 mosaic plus one extra central pointing; dividing that exposure time by 2.5 yields 5088 s within the central pointing.

the most distant galaxies known in future surveys. For RELICS results to date, see Section 6.2.

2.3. Galaxy Cluster Masses

Scaling relations linking mass estimates from lensing, X-ray, and SZ studies require understanding of observational systematics and scale-dependent cluster astrophysics. Improving the accuracy of these mass scaling relations will be key to realizing the full potential of future missions such as eROSITA, which anticipates detecting 100,000 clusters/groups out to $z \sim 1.3$ (Pillepich et al. 2018).

Constraints on cosmological parameters (primarily Ω_m and σ_8) derived from the *Planck* CMB (Planck Collaboration et al. 2016b) are at odds with those derived from *Planck* SZ galaxy cluster counts (Planck Collaboration et al. 2016c). The latter paper calibrated the scaling relation between *Planck* SZ signal strength and cluster masses based on analyses of *XMM-Newton* X-ray observations assuming hydrostatic equilibrium (HSE). One may expect cluster masses to be $\sim 20\%$ greater owing to deviations from HSE, including nonthermal pressure support (e.g., Nagai et al. 2007; Rasia et al. 2012). But Planck Collaboration et al. (2016c) found that the cosmology results can be reconciled only if one assumes that SZ-derived cluster

Table 5
Archival *HST* Imaging Programs of RELICS Clusters

Cluster Index	Abbreviated Name	Program ID	Principal Investigator	Filters
1	abell2163	12253	Clowe	F435W ^a , F606W ^a , F814W ^a
2	plckg287+32	14165	Seitz	F475W, F606W, F814W, F110W ^b
3	macs0417-11	12009	von der Linden	F606W ^c , F814W
5	rxs0603+42	13343	Wittman	F390W ^{a,c} , F606W ^a , F814W ^a
6	macs0308+26	12166	Ebeling	F606W
		12884	Ebeling	F814W
7	act0102-49	12477	High	F606W ^a , F814W
		12755	Hughes	F625W ^a , F775W ^a , F850LP ^a
8	rxs0600-20	12884	Ebeling	F814W
11	rxs2211-03	12166	Ebeling	F606W
13	plckg308-20	12884	Ebeling	F606W
14	rxs0018+16	9292	Ford	F775W, F850LP
		10493	Gal-Yam	F775W
		10635	Ziegler	F606W ^a
		11560	Ebeling	F555W, F814W
21	abell665	9292	Ford	F625W
22	macs0553-33	12362	Ebeling	F435W, F606W, F814W
23	smacs0723-73	12166	Ebeling	F606W
		12884	Ebeling	F814W
24	rxs0949+17	10491	Ebeling	F606W
		12166	Ebeling	F814W
25	abell1758	12253	Clowe	F435W ^a , F606W ^a , F814W ^a
27	abell2813	10881	Smith	F606W
28	abell520	12253	Clowe	F435W ^a , F606W ^a , F814W ^a
29	rxs0032+18	12166	Ebeling	F606W, F814W
31	abell3192	10881	Smith	F606W
		12313	Ebeling	F435W, F606W, F814W
32	macs0159-08	12166	Ebeling	F606W
33	macs0035-20	10491	Ebeling	F606W
		12884	Ebeling	F814W
34	rxs0911+17	9722	Ebeling	F555W, F814W
		10493	Gal-Yam	F814W
		10793	Gal-Yam	F814W
35	abell295	13514	Pacaud	F435W, F606W, F814W
36	spt0615-57	12477	High	F606W ^a , F814W
		12757	Mazzotta	F814W ^a
37	macs0257-23	9722	Ebeling	F555W, F814W
		10493	Gal-Yam	F814W
		10793	Gal-Yam	F814W
38	abell2537	9270	Allen	F606W
39	ms1008-12	9292	Ford	F775W, F850LP
		10635	Ziegler	F606W ^a
40	macs0025-12	10703	Ebeling	F555W, F814W
41	cl0152-13	9290	Ford	F625W ^a , F775W ^a , F850LP ^a
		10493	Gal-Yam	F775W
		10793	Gal-Yam	F775W

Notes.^a Multiple pointings with minimal or no overlap are given in superscript brackets.^b WFC3/IR observations obtained during the same *HST* Cycle as RELICS.^c WFC3/UVIS observations. (Other observations obtained prior to RELICS are all ACS.)

masses underestimate the true M_{500} masses by $b \approx 42\%$ (where they reported the mass bias as $1 - b = 0.58 \pm 0.04$). That is about 2σ greater than the $\sim 20\%$ initially adopted in the PSZ1 analysis (Planck Collaboration et al. 2014).

Weak-lensing analysis of clusters included in both the *Planck* analysis and the Weighing the Giants survey (WtG; von der Linden et al. 2014b) shows that *Planck* cluster masses may indeed be underestimated by $\sim 42\%$ for the most massive clusters ($>10^{15} M_{\odot}$), while *Planck* masses appear to be more accurate for less massive clusters ($\sim 5 \times 10^{14} M_{\odot}$). Subsequent weak-lensing analyses from various surveys (WtG, CCCP, LoCUSS, CLASH, CFHTLenS, RCSLenS, HSC-SSP) found a range of results, some consistent with WtG including bias increasing with mass (Sereno & Ettori 2017), and others more consistent with the original *Planck* estimate of $\sim 20\%$ bias (Hoekstra et al. 2015; Battaglia et al. 2016; Smith et al. 2016; Penna-Lima et al. 2017; Medezinski et al. 2018). Overall, the tension appears to be somewhat relieved, although not conclusively (Planck Collaboration et al. 2018b), especially after accounting for new *Planck* measurements of the reionization optical depth (Planck Collaboration et al. 2016e, 2018a).

SZ mass estimates are calibrated in part based on X-ray temperatures measured with spectroscopy out to r_{500} , which can be difficult, especially for higher-redshift clusters. X-ray mass calibration at the smaller r_{2500} radii probed by *HST* strong lensing may be key to improving mass scaling relations. These smaller radii are also important for ground-based SZ telescopes offering significantly higher resolution than *Planck*. Czikon et al. (2015) analyzed arcsecond-resolution Bolocam SZ imaging of 45 clusters and found that the Y_{SZ} signal does not scale self-similarly with M_{2500} derived from X-ray observations. The cause of this mismatch may be due to AGN feedback regulating star formation and altering the gas properties in cluster cores. Through accurate lensing mass profiles measuring total mass, free from the assumption of gas HSE, and accurate gas mass profiles from *Chandra*, we will determine the radial dependence of $f_{\text{gas}} = M_{\text{gas}}/M_{\text{tot}}$ and characterize the efficiency with which AGNs input energy into the intracluster medium.

Long-term efforts to improve mass scaling relations focus on weak-lensing analyses, for example, from Euclid and LSST (Grandis et al. 2019). However, strong-lensing analyses will also contribute. Simulations have shown that joint strong-lensing + weak-lensing analyses yield significantly smaller biases ($\sim 2\%$) and uncertainties ($\sim 20\%$) in virial mass estimates than either weak or strong lensing alone (Meneghetti et al. 2010). A joint strong-lensing plus weak-lensing analysis of 20 CLASH clusters based on *HST* and Subaru observations (Umetsu et al. 2016) shows that the M_{2500} masses can be determined with a fractional total uncertainty of 25% per cluster at $\langle M_{2500} \rangle = 3.6 \times 10^{14} M_{\odot}$ (or $\langle M_{500} \rangle = 10^{15} M_{\odot}$), accounting for the dominant contributions from intrinsic profile variations (Gruen et al. 2015). Thus, a similar analysis of all 41 RELICS clusters would yield an overall mass calibration accuracy of about 4% from r_{2500} out to the virial radii, providing a legacy mass profile database for critical tests for models of background cosmology and structure formation.

2.4. Dark Matter Constraints

Self-interacting dark matter (SIDM) particles with cross sections of $\sigma_{\text{DM}}/m \sim 0.1\text{--}0.6 \text{ cm}^2 \text{ g}^{-1}$ have been invoked to explain several observational inconsistencies with collisionless

Table 6
RELICS *HST* Imaging with ACS and WFC3

Cluster Index	Abbreviated Name	Cluster F435W (orbits)	F606W (orbits)	F814W (orbits)	WFC3/IR (orbits)	Parallel WFC3 (orbits)	Time between WFC3 Epochs (days)
1	abell2163				4 ^a		40
2	plckg287+32 ^b	1	*	*	2		25
3	macs0417-11	1			2		40
4	abell697	1	1	1	2	3	41
5	rxs0603+42				4 ^a		37
6	macs0308+26	1	0.5	0.5	2		25
7	act0102-49	1			4 ^a		31
8	rxs0600-20	1	1	1	2	3	39
9	plckg209+10	1	1	1	2	3	42
10	plckg171-40	1	1	1	2	3	41
11	rxs2211-03	1	1	1	2	3	40
12	plckg004-19	1	1	1	2	3	41
13	plckg308-20	1	1	1	2	3	42
14	rxs0018+16	1			2		61
15	spt0254-58	1	1	1	2	3	40
16	plckg138-10	1	1	1	2	3	41
17	rxs0142+44	1	1	1	2	3	41
18	abell1300	1	1	1	2	3	43
19	whl0137-08	1	1	1	2	3	40
20	rxs1514-15	1	1	1	2	3	40
21	abell665	1	1	1	2	3	49
22	macs0553-33				2		40
23	smacs0723-73	1	0.5	0.5	2+6		40 ^c
24	rxs0949+17	1	0.5	0.5	2		42
25	abell1758				4 ^a		43
26	abell1763	1	1	1	2+7	3	40 ^c
27	abell2813	1	1	1	2	3	40
28	abell520				4 ^a		42
29	rxs0032+18	1	0.5	0.5	2		56
30	rxs0232-44	1	1	1	2	3	40
31	abell3192				2		40
32	macs0159-08	1	1	1	2	3	36
33	macs0035-20	1	0.5	0.5	2		63
34	rxs0911+17	1			2		49
35	abell295				2		40
36	spt0615-57	1			2		40
37	macs0257-23	1			2		41
38	abell2537	1		1	2		41
39	ms1008-12	1			2		42
40	macs0025-12	1			2		25
41	cl0152-13	1			2+5		43 ^c

Notes.^a Observations were split between two pointings.^b PLCK G287+32 was also awarded Cycle 23 observations under GO 14165 (PI Seitz). In addition to the four ACS orbits in F475W, F606W, and F814W listed in Table 4, that program also obtained four orbits (10,447 s) of WFC3/IR F110W imaging. RELICS observed this cluster in ACS F435W and WFC3/IR F105W, F125W, F140W, and F160W, relinquishing the two awarded orbits of F606W and F814W imaging that would have been duplicated.^c Indicates WFC3 orbits added for SN follow-up observations (Table 7). For those clusters, “Time between WFC3 Epochs” refers to the first two epochs.

cold dark matter (CDM) theory, including galaxy cluster density profiles, “missing” Milky Way satellites, and the “cusp–core” problem (see Robertson et al. 2019 and references therein). Baryonic processes can explain these “problems” with varying degrees of success. Merging galaxy clusters yield the most robust constraints on SIDM. As two clusters collide, galaxies pass straight through the collision, leaving the stripped cluster gas lagging behind. We expect dark matter to also pass straight through unless the particles have a significant self-interacting cross section. Joint *HST* lensing plus *Chandra* X-ray analysis of the Bullet Cluster (Clowe et al. 2006; Bradač et al. 2006)

constrained $\sigma_{\text{DM}}/m < 1.25 \text{ cm}^2 \text{ g}^{-1}$ (68% confidence; Randall et al. 2008). More recently, Harvey et al. (2015) improved this constraint to $\sigma_{\text{DM}}/m < 0.47 \text{ cm}^2 \text{ g}^{-1}$ (95% confidence) by jointly analyzing *HST* + *Chandra* imaging of 30 cluster mergers (Bradač et al. 2008; Dawson et al. 2012). However, Wittman et al. (2018) subsequently analyzed more data (including more *HST* filters) on these same 30 clusters and claimed that the constraint should be more relaxed: $\sigma_{\text{DM}}/m \lesssim 2 \text{ cm}^2 \text{ g}^{-1}$.

RELICS includes seven cluster mergers analyzed by these papers plus another 17 confirmed plus nine possible mergers not in their sample. Of the confirmed mergers, all but one have

Table 7
HST WFC3/IR and UVIS Follow-up Imaging of RELICS Supernovae

Cluster	Supernova	Total Orbits	F105W	F125W	F140W	F160W	F350LP
abell1763	Nebra	7	0.3	2.7		3.7	0.3
clj0152-13	Nimrud	5		2.5		2.5	
smacs0723-73	Yupana	6	2	1	2	1	

Note. The full list of RELICS SN discoveries is given in Table 18.

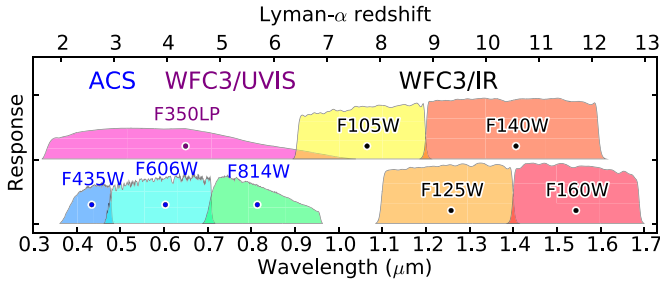


Figure 3. RELICS clusters were observed with the seven *HST* ACS and WFC3/IR filters shown here. RELICS parallels were observed with the one WFC3/UVIS and four WFC3/IR filters shown. Response curves are plotted vs. wavelength (λ), with the corresponding Ly α redshift (z) given along the top axis ($\lambda = 0.1216\mu\text{m} (1+z)$). F350LP, F105W, and F140W are offset vertically for clarity. Black dots mark the effective “pivot” wavelengths (Tokunaga & Vacca 2005) of the filters.

existing *Chandra* imaging. Joint analyses of the lens models plus X-ray data of these massive cluster mergers (specifically, those observed post-merger) will help constrain the SIDM parameter space toward the astrophysically and theoretically interesting limit of $0.1 \text{ cm}^2 \text{ g}^{-1}$.

2.5. Supernovae

Large *HST* programs have yielded many distant SNe. CLASH and CANDELS discovered both Type Ia SNe (SNe Ia) and core-collapse SNe (CCSNe) out to $z = 2.5$. The observed SN Ia rates suggest that Type Ia progenitors are primarily double white dwarf systems (Graur et al. 2014) that do not explode quickly after formation (Rodney et al. 2014). High- z CCSN rates from these programs reinforced measurements of the cosmic star formation rate history and put constraints on the initial mass function for CCSN progenitors (Stroger et al. 2015).

Lensed SNe Ia from CLASH and the Frontier Fields provided the first empirical tests verifying the accuracy of lens model magnification estimates (Nordin et al. 2014; Patel et al. 2014; Rodney et al. 2015b). The appearance of “SN Refsdal” (Kelly et al. 2015) was the first strongly lensed SN observed as multiple images with measurable time delays (Rodney et al. 2016b). These time delays can be used to test lens models (Kelly et al. 2016; Treu et al. 2016) or as a cosmological distance measurement (Grillo et al. 2018; Vega-Ferrero et al. 2018). Strong-lensing clusters have also revealed other faint transient phenomena, including extreme magnifications of individual stars or stellar eruptions in galaxies at $z = 1.49$ (Kelly et al. 2018), $z = 1.01$ (Rodney et al. 2018), and $z = 0.94$ (Chen et al. 2019; Kaurov et al. 2019).

RELICS observed each cluster in two epochs separated by ~ 40 days to identify SNe and other transient phenomena. This cadence was designed to catch $z \sim 1$ –2 SNe near peak brightness in epoch 2. Our primary goal was to significantly

Table 8
 Nominal Exposure Times and Expected Depths

Camera	Filter	λ^a (μm)	Exp. ^b Time	Depth ^c (AB)	Sens. ^d (nJy)
<i>HST</i> ACS/WFC	F435W	0.43	1952 s	27.2	9
<i>HST</i> ACS/WFC	F606W	0.59	1991 s	27.6	7
<i>HST</i> ACS/WFC	F814W	0.81	2123 s	27.1	11
<i>HST</i> WFC3/IR	F105W	1.06	1361 s	26.6	16
<i>HST</i> WFC3/IR	F125W	1.25	686 s	26.0	29
<i>HST</i> WFC3/IR	F140W	1.39	686 s	26.2	25
<i>HST</i> WFC3/IR	F160W	1.54	1861 s	26.5	19
<i>SST</i> IRAC	ch1	3.6	5 hr	25.0	76
<i>SST</i> IRAC	ch2	4.5	5 hr	24.6	108

Notes.

^a Effective “pivot” wavelength (Tokunaga & Vacca 2005).

^b Total integration times for A1763; slightly longer integrations were obtained for most other clusters. Much deeper *SST* integrations (30 hr) were obtained for 10 RELICS clusters.

^c 5σ point-source AB magnitude limit. *HST*: within a $0''.4$ diameter aperture assuming exposure time is split into four integrations. *SST*: assuming medium background with 180 integrations of 100 s each.

^d 1σ point-source sensitivity (nJy) within the same apertures.

contribute to the numbers of known distant and lensed SNe discovered in previous surveys. Ultimately, RELICS discovered 11 SNe (Section 6.3). The RELICS proposal included 20 orbits for follow-up imaging to confirm and obtain light curves for the more interesting candidates. RELICS observations will also provide a baseline for the longer-term (decade) monitoring required to detect higher-redshift SNe and other lensed transients, perhaps including individual Population III stars (Windhorst et al. 2018).

3. Galaxy Clusters

RELICS observed the 41 massive galaxy clusters at $0.182 \leq z \leq 0.972$ listed in Tables 2 and 3. None had existing *HST* infrared imaging (WFC3/IR or NICMOS) prior to RELICS. As shown in Figure 1, we selected 21 of the clusters based on exceptionally high mass estimates from *Planck* and the other 20 based on other factors revealing or suggesting exceptional lensing strength, including details noted in Table 3.

Planck Collaboration et al. (2016a) identified 1653 SZ (Sunyaev & Zeldovich 1970) sources in their PSZ2 all-sky ($|b| > 15^\circ$) catalog,³⁶ including 1203 confirmed clusters, 1094 of which had measured redshifts and SZ mass estimates. A few hundred of these were newly discovered clusters, including some of the most massive known.

³⁶ *Planck* PSZ2 catalogs are available and described at http://irsa.ipac.caltech.edu/data/Planck/release_2/catalogs/ and <https://wiki.cosmos.esa.int/planckpla2015/index.php/Catalogues>

Table 9Nominal *HST* Exposures for a Cluster and Parallel Field with No Archival Imaging

Epoch/ Orbit	Dither ^a Position	Prime Filter	Exposure Time (s)	Parallel Filter	Exposure Time (s)
1/1	A	F435W	370	F350LP	454
1/1	B	F435W	667	F350LP	701
1/1	C	F435W	667	F350LP	701
1/1	D	F435W	371	F350LP	496
1/2	A	F814W	516	F140W	603
1/2	B	F814W	607	F105W	703
1/2	C	F814W	607	F160W	703
1/2	D	F814W	516	F125W	603
1/3	W	F140W	178		
1/3	W	F105W	353		
1/3	Y	F105W	353		
1/3	Y	F140W	178		
1/3	Z	F125W	178		
1/3	Z	F160W	503		
1/3	X	F160W	503		
1/3	X	F125W	153		
2/4	A	F606W	516	F125W	503
2/4	B	F606W	607	F160W	703
2/4	C	F606W	607	F105W	703
2/4	D	F606W	516	F140W	503
2/5	Z	F140W	178		
2/5	Z	F105W	353		
2/5	X	F105W	353		
2/5	X	F140W	203		
2/5	W	F125W	178		
2/5	W	F160W	503		
2/5	Y	F160W	453		
2/5	Y	F125W	230		

Notes. Each epoch begins with ACS on the prime cluster field and WFC3 in parallel and ends with WFC3/IR in prime. Epochs 1 and 2 are separated by about a month, or longer when possible.

^a Each ACS dither position (ABCD) takes another step across the chip gap. The WFC3/IR dither positions consist of two close ($\sim 0''.8$) pairs (WX and YZ) separated by a larger distance ($\sim 6''.5$) to cover the “death star.”

Table 10
Spitzer IRAC Imaging Programs

Program	PI	TAC	Hours ^a	Depth ^b	Clusters ^c
12005	Bradač	GO	99.9	1.2	26
12123	Soifer	DDT	290	5	34
13165	Bradač	DDT	167	30	3
13210	Bradač	DDT	55.5	30	1
14017	Bradač	GO	333.2	30	6

Notes.

^a Total hours awarded, including overheads.

^b Resulting total hours observed in each IRAC filter (ch1, ch2) for each cluster, including previous observations.

^c Number of RELICS clusters observed. The first two programs observed all clusters as required to reach target depths. The final three programs observed 10 clusters to achieve 30 hr depth for each.

We queried the *HST* observations of all the *Planck* clusters using the Mikulski Archive for Space Telescopes (MAST).³⁷ Many had existing *HST* imaging prior to RELICS, but many more did not.

The 34 most massive clusters ($M_{500} > 8.8 \times 10^{14} M_{\odot}$) include some already well studied by *HST* and *Spitzer*, including 4/6 Frontier Fields clusters³⁸ and 5/25 from CLASH (with three common to both surveys). But others were less well studied. Nine of the top 34 had yet to be observed by *HST* or *Spitzer* at all, and 12 more had yet to be observed by *HST* in the near-infrared with NICMOS or WFC3. These 21 clusters compose half of the RELICS sample; RELICS obtained the first *HST* infrared imaging of these clusters, and *Spitzer* imaging as needed.

The remaining 20 RELICS clusters are primarily known strong lenses based on existing *HST* optical imaging (or ground-based imaging in the case of RXC 0232-44; Kausch et al. 2010). Existing *HST* ACS imaging, where available, reduced our total orbit request. We also considered other factors in this selection, including X-ray mass estimates (Mantz et al. 2010; MCXC Piffaretti et al. 2011), weak-lensing mass estimates (Sereni 2015 compilation including Weighing the Giants; Applegate et al. 2014; von der Linden et al. 2014a; Umetsu et al. 2014; Hoekstra et al. 2015), SDSS clusters (Wen et al. 2012; Wong et al. 2013), and other SZ mass estimates from SPT (Bleem et al. 2015) and ACT (Hasselfield et al. 2013), as well as clusters nearly selected for the Frontier Fields.³⁹

The 41 RELICS clusters generally bear the names of the surveys that discovered them: Abell (1958); Abell et al. (1989); the Einstein Observatory Extended Medium-Sensitivity Survey (MS; Gioia et al. 1990); the *ROSAT* X-ray All-Sky Galaxy Cluster Survey (RXC; Ebeling et al. 1998, 2000a); the *ROSAT* Massive Cluster Survey (MACS and SMACS; Ebeling et al. 2001, 2007, 2010, 2013; Mann & Ebeling 2012; Repp et al. 2016; Repp & Ebeling 2018); an extended radio source discovered in *ROSAT* (RXS; van Weeren et al. 2012); the Wen, Han, & Liu SDSS-III cluster catalog (WHL; Wen et al. 2012); the South Pole Telescope SZ survey (SPT; Bleem et al. 2015); the Atacama Cosmology Telescope SZ survey (ACT; Hasselfield et al. 2013); and the *Planck* all-sky SZ survey (*Planck* Collaboration et al. 2011, 2016a). CL J0152.7–1357 at $z = 0.833$ was discovered by Ebeling et al. (2000b) in the Wide Angle *ROSAT* Pointed Survey (WARPS). Alternate cluster names include one also identified in the Rosat Bright Survey (RBS; Kausch et al. 2010) and another in Clusters in the Zone of Avoidance (CIZA; Kocevski et al. 2007).

The Abell clusters are numbered sequentially based on the original catalog. Numbers in other cluster names codify coordinates, often in J2000 R.A. HH:MM and decl. DD:MM. *Planck* cluster names, instead, give Galactic coordinates in longitude and latitude. Table 3 lists names and any alternate names for each RELICS target. Their positions on the sky are shown in Figure 2.

4. Observations

All data from our large *HST* and *Spitzer* observing programs had no proprietary period. We describe each of these programs

³⁸ The Frontier Fields cluster A370 has a lower *Planck* mass $M_{500} = 7.7 \times 10^{14} M_{\odot}$ (though weak-lensing analysis yields a far greater $M_{500} = 1.9 \times 10^{15} M_{\odot}$; Umetsu et al. 2011). MACS J0416.1-2403 is PSZ2 G221.06-44.05, but the association was not initially made; without the redshift, no mass estimate was possible in the PSZ2 catalog. However, the relatively low *Planck* signal-to-noise ratio of 5.2 suggests a lower mass.

³⁹ <https://outerspace.stsci.edu/display/HPR/Frontier+Fields+Cluster+Candidate+Selection>

³⁷ <http://archive.stsci.edu/hst/search.php>

Table 11
Large Surveys Including RELICS Clusters Motivated in Part by RELICS

Name	PI	Observatory	Instrument	Time	Wavelength	RELICS/Total Clusters
RELICS ^a	Coe	<i>HST</i>	ACS, WFC3	115 hr	0.4–1.7 μm	41
S-RELICS ^b	Bradač; Soifer	<i>Spitzer</i>	IRAC	945 hr	3–5 μm	34 ^c
GAME	Mercurio	VST	OmegaCAM	300 hr	ugri	9/12
GCAV ^d	Nonino	VISTA	VIRCAM	540 hr	YJKs	13/20
Witnessing ^e	Arnaud & Etti	<i>XMM-Newton</i>	EPIC	833 hr	0.15–15 keV	18/118
ALCS	Kohn	ALMA	12 m array	95 hr	1.1 mm	16/33
Probing ^f	van Weeren	VLA	25 m array	85 hr	2–4 GHz	34 ^g

Notes. The RELICS clusters were observed by many previous programs, including MACS *HST* snapshot programs and large *Spitzer* programs (see Section 1). This table does not include those, instead summarizing the more recent programs inspired in part by the RELICS program.

^a <https://relics.stsci.edu>

^b <https://irsa.ipac.caltech.edu/data/SPITZER/SRELICS/overview.html>

^c The remaining seven RELICS clusters already had archival 5 hr depth, and none of them were targeted for 30 hr depth.

^d <http://archive.eso.org/cms/eso-archive-news/first-data-release-from-the-galaxy-clusters-at-vircam-gcav-eso-vista-public-survey.html>

^e Witnessing the culmination of structure formation in the universe.

^f Probing cosmic star formation with the JVLA Lensing Cluster Survey.

^g All RELICS clusters accessible to VLA.

in turn, followed by other subsequent large observing programs of RELICS clusters.

4.1. HST Imaging

Of the 41 RELICS clusters, 28 had been observed previously by *HST* with ACS and/or WFC3/UVIS (Tables 4 and 5). Our 188-orbit *HST* Treasury Program (Cycle 23; GO 14096; PI Coe; Deputy PI Bradley) obtained additional observations with ACS and WFC3/IR (Table 6). Five clusters required two WFC3/IR pointings for a total of 46 new WFC3/IR images of strongly lensed fields. For each field, we observed two orbits of WFC3/IR split among four filters: F105W, F125W, F140W, and F160W (Figure 3). And for each cluster, we observed three orbits of ACS split among F435W, F606W, and F814W, minus any archival imaging. For the 18 RELICS clusters without any existing ACS imaging, we observed the full three orbits of ACS and, in parallel, three orbits of WFC3 on a blank field: one orbit of WFC3/UVIS F350LP and two orbits of WFC3/IR F105W, F125W, F140W, and F160W. The parallels use the same filters as in BoRG[z9–10] (Calvi et al. 2016; Morishita et al. 2018), adding area to our high- z search.

For each cluster, we split the observations into two epochs separated by 25–63 days (typically ~ 40 ; see Table 6). This enabled searches for SNe and other transients. Twenty orbits of RELICS were allocated to follow up such Targets of Opportunity (ToO). We executed these orbits on three of the nine SNe discovered by RELICS (Table 7).

Total integration times for each *HST* orbit vary with the time available between Earth occultations and the time to acquire or reacquire guide stars. Table 8 gives the total integration times in each filter for A1763, as a representative example. For most other clusters, the integration times were slightly longer (by up to 15%). Each integration was split into four exposures at different dither positions (pointings). We dithered across the ACS chip gap and WFC3/IR “death star” to fill these gaps in the data.

Table 9 gives the detailed breakdown of epochs, orbits, and exposure times at each of the four dither positions in each filter for a nominal target with no archival imaging. In the parallel fields, note that the WFC3/UVIS F350LP imaging consists of

four exposures at four dither positions, but the parallel WFC3/IR imaging consists of only two exposures in each filter (one per epoch).

4.2. Spitzer Imaging

Altogether, RELICS has been awarded 945 hr of *Spitzer* observing time (Table 10). For each cluster, we obtained IRAC imaging as needed in the two warm mission filters, ch1 (3.6 μm) and ch2 (4.5 μm). Combined, these filters span approximately 3–5 μm . About 100 hr of archival IRAC imaging were also available for 18 of the clusters in these two filters, most notably from GO 60034 (PI Egami). Below we summarize the complete *Spitzer* RELICS data sets, which will be detailed further by V. Strait et al. (2019, in preparation).

Our initial 100 hr SRELICS (*Spitzer* RELICS) program (Cycle 12; GO 12005; PI Bradač) was supplemented by a 290 hr Director’s Discretionary Time program (DDT 12123; PI Soifer). Combined, these programs observed all RELICS clusters (as needed) to achieve a total of 5 hr of integration time (combining new and archival imaging) in each of the two IRAC filters. The five clusters requiring two WFC3/IR pointings also required two IRAC pointings.

Subsequently, based on our analyses of the *HST* and *Spitzer* images, we were awarded three more proposals (PI Bradač) to obtain deeper IRAC imaging (30 hr/band), requiring an additional 556 hr on the 10 clusters yielding the most high- z candidates at $z \sim 6$ –10 (Salmon et al. 2017, 2018). DDT 13165 observed PLCK G287.0+32.9, PLCK G004.5–19.5, and A1763. DDT 13210 observed SPT-CL J0615–5746 and the $z \sim 10$ arc discovered by Salmon et al. (2018). And GO 14017 observed CL J0152.7–1357, ACT-CL J0102–49151, PLCK G308.3–20.2, RXS J060313.4+421, MS 1008.1–1124, and SMACS J0723.3–7327.

4.3. Other Large Surveys of RELICS Clusters

In addition to the large *HST* and *SST* observing programs, RELICS has also motivated large surveys with other telescopes, including VST, VISTA, *XMM-Newton*, ALMA, and VLA (see Table 11). The VLA survey exclusively observes RELICS clusters, while the other listed programs have most or

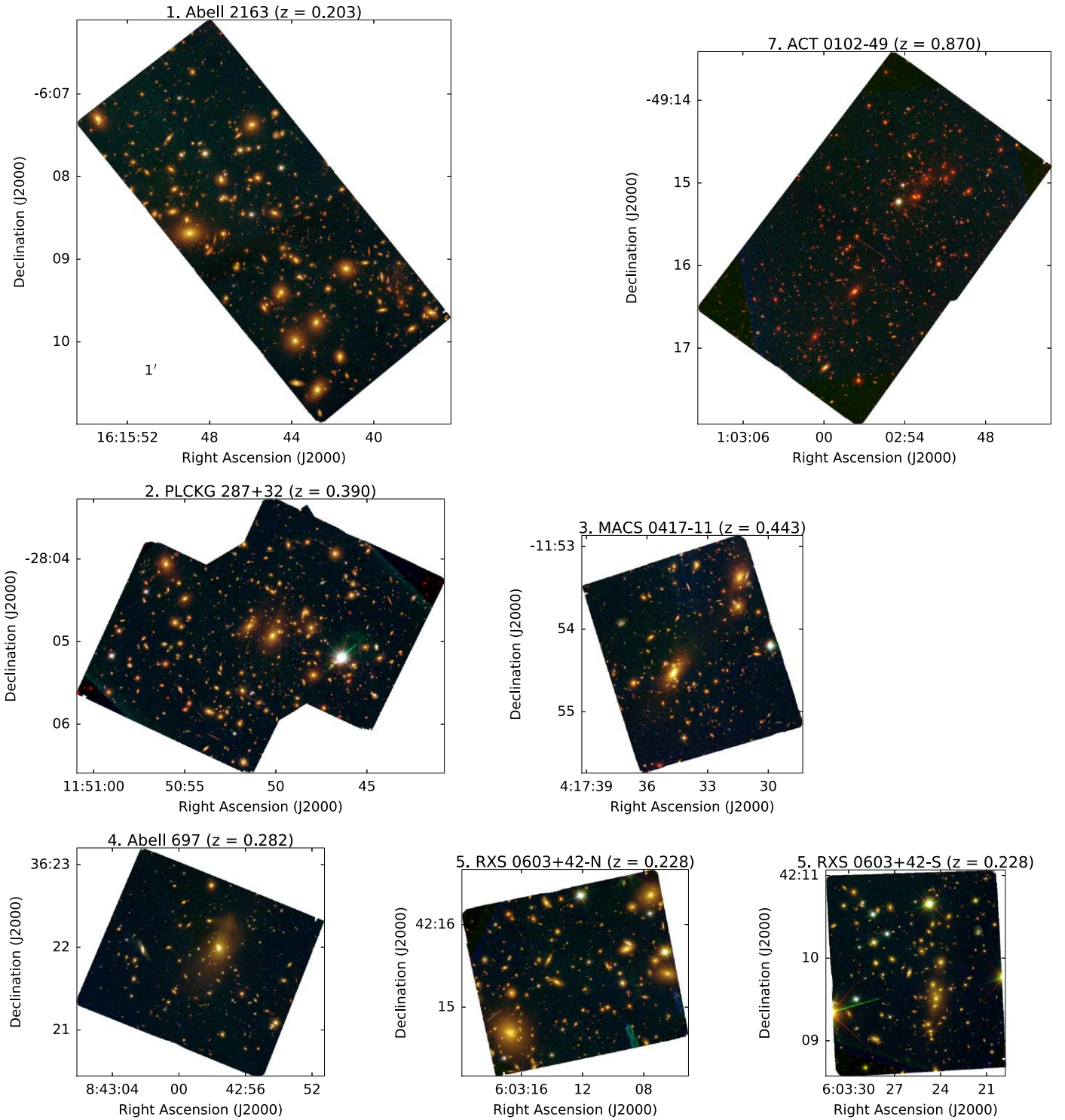


Figure 4. *HST* ACS + WFC3/IR observations of RELICS clusters within the WFC3/IR footprints. ACS imaging extends to wider areas not shown. All images are shown to the same scale. North is up; east is left. Color images produced using Trilogy (Coe et al. 2012): blue = F435W; green = F606W + F814W; red = F105W + F125W + F140W + F160W.

just some clusters in common with RELICS. We have also carried out smaller follow-up programs with many other observatories, including Keck MOSFIRE and DEIMOS, VLT MUSE and X-SHOOTER, Gemini GMOS, Subaru Suprime-Cam and HSC, Magellan MegaCam and LDSS3, MMT Hectospec, and GMRT. Spectra from Magellan LDSS3 have

already been used in several papers (Cerny et al. 2018; Paterno-Mahler et al. 2018; Mainali et al. 2019). Also note that while we are advertising these newer surveys here, we also emphasize that many RELICS clusters have been observed previously by large programs carried out with *HST*, *Spitzer*, *Chandra*, *XMM-Newton*, and ground-based observatories.

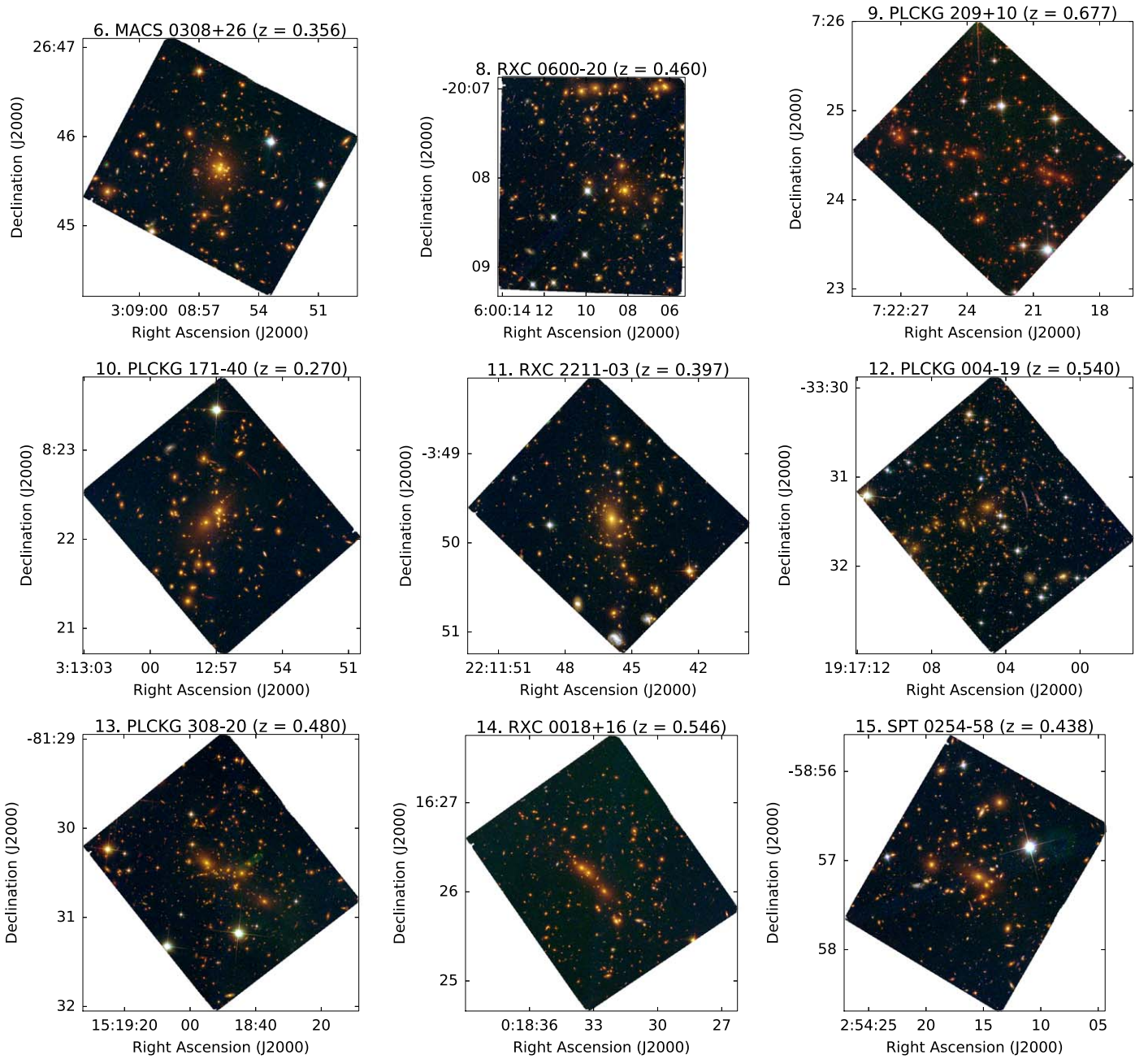


Figure 4. (Continued.)

5. Image Reductions and Catalogs

We have made our *HST* reduced images and catalogs publicly available via MAST⁴⁰ at doi:10.17909/T9SP45 and our *Spitzer* reduced images available via IRSA.⁴¹ Below we describe the procedures used to generate these data products.

5.1. HST Image Reductions

We reduced all *HST* images obtained by RELICS and all archival *HST* ACS and WFC3/IR images that overlap with the RELICS WFC3/IR images. Our *HST* image reduction procedure is similar to that performed on the Frontier Fields *HST* images

(Lotz et al. 2017). Key differences are that we do not produce “self-calibrated” ACS images (due to insufficient numbers of exposures), nor do we correct for time-variable sky emission due to helium line emission at $1.083\ \mu\text{m}$, which occasionally affects WFC3/IR F105W images (Brammer et al. 2014).

We correct all *HST* images for bias, dark current, and flat fields with up-to-date reference files (as noted in the FITS headers of our final reduced images). We manually identified and masked any satellite trails. ACS images were corrected for charge transfer efficiency (CTE) and bias striping. The multiple ACS exposures were used to automatically identify and reject cosmic rays. Each WFC3/IR MULTIACCUM exposure consists of multiple samples, enabling “up-the-ramp” cosmic-ray rejection. We also masked bad pixels using updated identifications in WFC3/IR images from GO 14114 (G. Brammer 2019, private communication).

⁴⁰ <https://archive.stsci.edu/prepds/relics/>

⁴¹ <https://irsa.ipac.caltech.edu/data/SPITZER/SRELICS/>

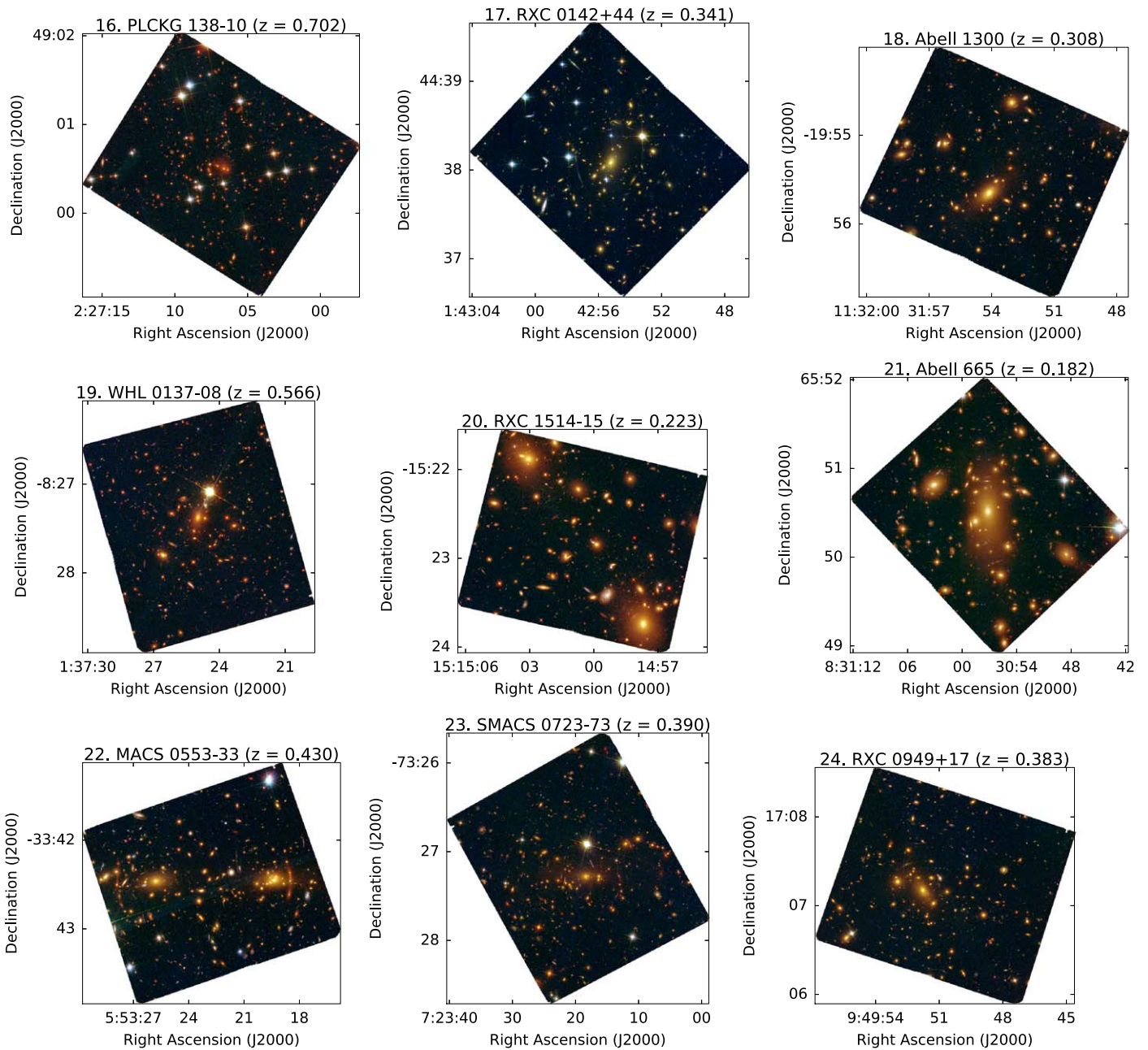


Figure 4. (Continued.)

We produced inverse variance maps (IVMs) quantifying the uncertainty in each pixel before accounting for correlated pixel noise (an additional 10%–15%) and Poisson source noise. These IVMs were used as weights to drizzle-combine the images obtained in each filter.

For each cluster or parallel field, we aligned all processed *HST* images to two common grids with $0''.06$ and $0''.03$ resolution. These are meant to adequately sample the point-spread functions (PSFs) in the WFC3/IR images ($\text{FWHM} \sim 0''.18$) and ACS images ($\text{FWHM} \sim 0''.09$), respectively. We used procedures from DrizzlePac, specifically AstroDrizzle (Gonzaga et al. 2012), and as outlined in Koekemoer et al. (2002, 2011) and Lotz et al. (2017). We set the drizzle parameter `pixfrac` = 0.8, as used in programs such as CANDELS (see discussion in Section 5.8.2 of Koekemoer et al. 2011).

We corrected the absolute astrometry of our images using the *Wide-field Infrared Survey Explorer* (WISE) point-source catalog (Wright et al. 2010).

Finally, we produced automatically scaled color images using Trilogy (Coe et al. 2012). Figure 4 show *HST* ACS + WFC3 color images of all 46 WFC3/IR cluster fields observed by RELICS. The ACS color images extend to wider areas, which are not shown here but are available on MAST. Also on MAST are color images of the 18 RELICS parallel fields observed with WFC3 UVIS and IR.

5.2. HST Detection and Photometry Catalogs

Based on the $0''.06$ resolution *HST* images, we produced source catalogs using techniques similar to those employed for the public

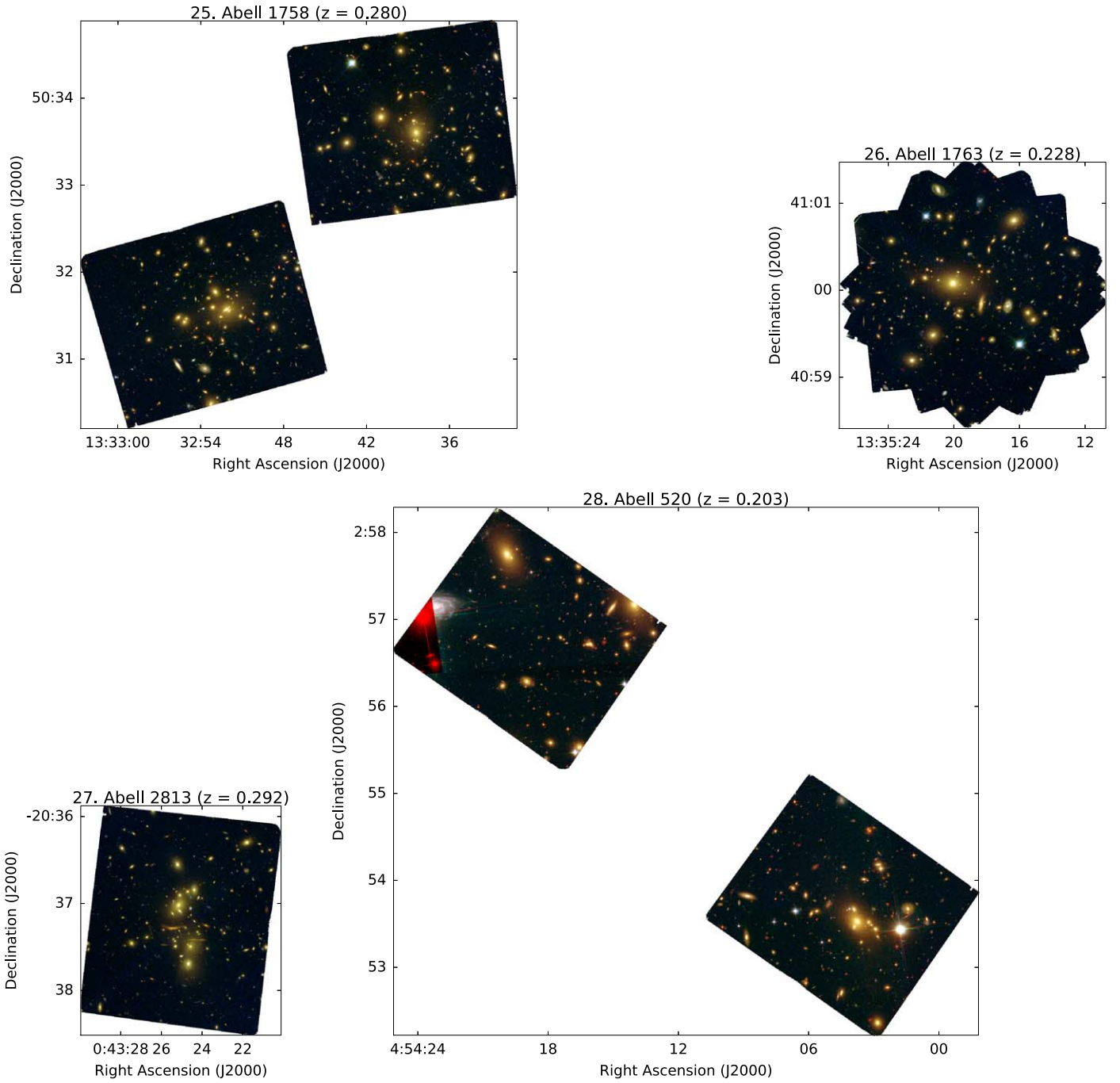


Figure 4. (Continued.)

CLASH catalogs (Postman et al. 2012; Coe et al. 2013) and the Frontier Fields analysis presented in Coe et al. 2015.

We ran SExtractor (Bertin & Arnouts 1996) version 2.8.6 in dual-image mode to detect objects in each field and define their isophotal apertures for photometry to be measured in each filter image. For each field, we produce two source catalogs:

1. *acs-wfc3* (or *acs-wfc3ir*): based on detections in a weighted stack of all *HST* images (ACS, WFC3/UVIS, and WFC3/IR), optimized to detect most objects.
2. *wfc3ir*: based on detections in a weighted stack of WFC3/IR images only using a finer background grid and

more aggressive deblending, optimized to detect smaller high-redshift galaxies.

The stacked images are weighted sums; the weights are the IVMs produced by the drizzling software (Section 5.1). For SExtractor input, we also produce rms maps equal to $1/\sqrt{\text{weight}}$.

Table 12 lists the SExtractor parameters used for the *acs-wfc3* and *wfc3ir* catalogs. The latter is geared toward detections of small high-redshift galaxies, so we use a smaller background grid and more aggressive deblending to detect small objects near brighter ones. The *acs-wfc3* catalogs

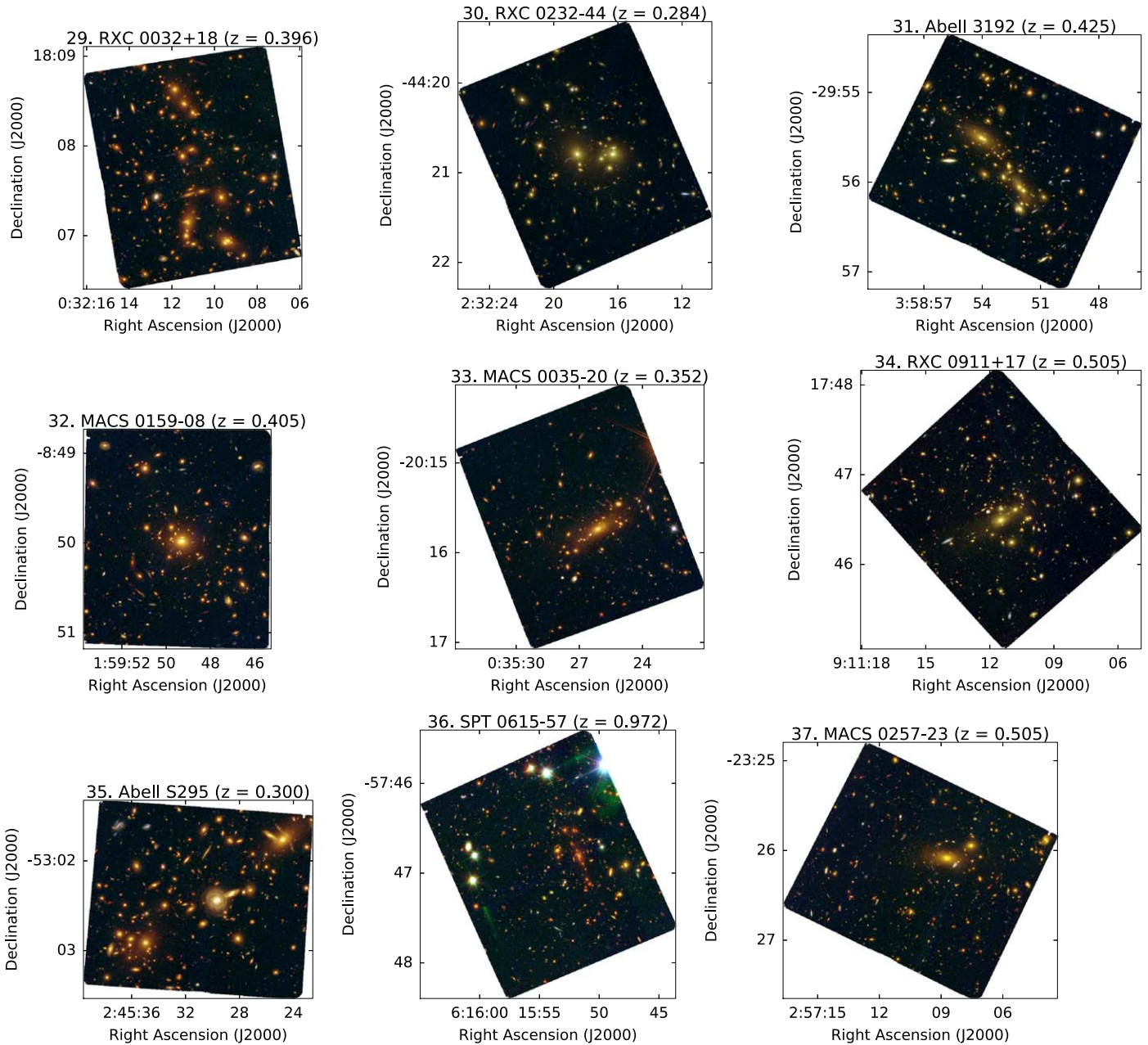


Figure 4. (Continued.)

cover the full (larger) ACS field of view and aim to detect whole objects, breaking them apart less often.

For detections in either catalog, 9 contiguous pixels are required at the level of the observed background rms or higher. The `acs-wfc3(wfc3ir)` background is calculated in 5×5 (3×3) grids of cells with 128×128 (64×64) pixels in each cell. We set the deblending of adjacent objects to 128 (64) levels of 0.0015 (0.0001) minimum contrast.

Each object's detection defines an isophotal aperture, which SExtractor uses in dual-image mode to measure isophotal photometry in every filter in the aligned images. Just outside this aperture, we have SExtractor use a 24-pixel-wide rectangular annulus around each object to estimate and subtract the local background in each filter. We do not perform aperture corrections, as the PSF FWHMs only vary between $\sim 0''.07$ and

$0''.15$ and we use relatively large isophotal apertures (see discussion in Postman et al. 2012, Section 5.1).

Finally, we correct all photometry for Galactic extinction using the IR dust emission maps of Schlafly & Finkbeiner (2011).⁴² Table 2 gives the extinction $E(B - V)$ for each cluster from those maps. These are multiplied by coefficients A_λ (Table 13) for each filter to determine the extinction in magnitudes.

Table 14 summarizes the output in our *HST* catalogs available on MAST. Samples are provided from our A697 IR-detection catalog for object detection and shape measurement (Table 15), photometry (Table 16), and Bayesian photometric redshifts (Table 17), which are discussed below.

⁴² Dust extinctions extracted using <http://irsa.ipac.caltech.edu/applications/DUST/docs/dustProgramInterface.html>.

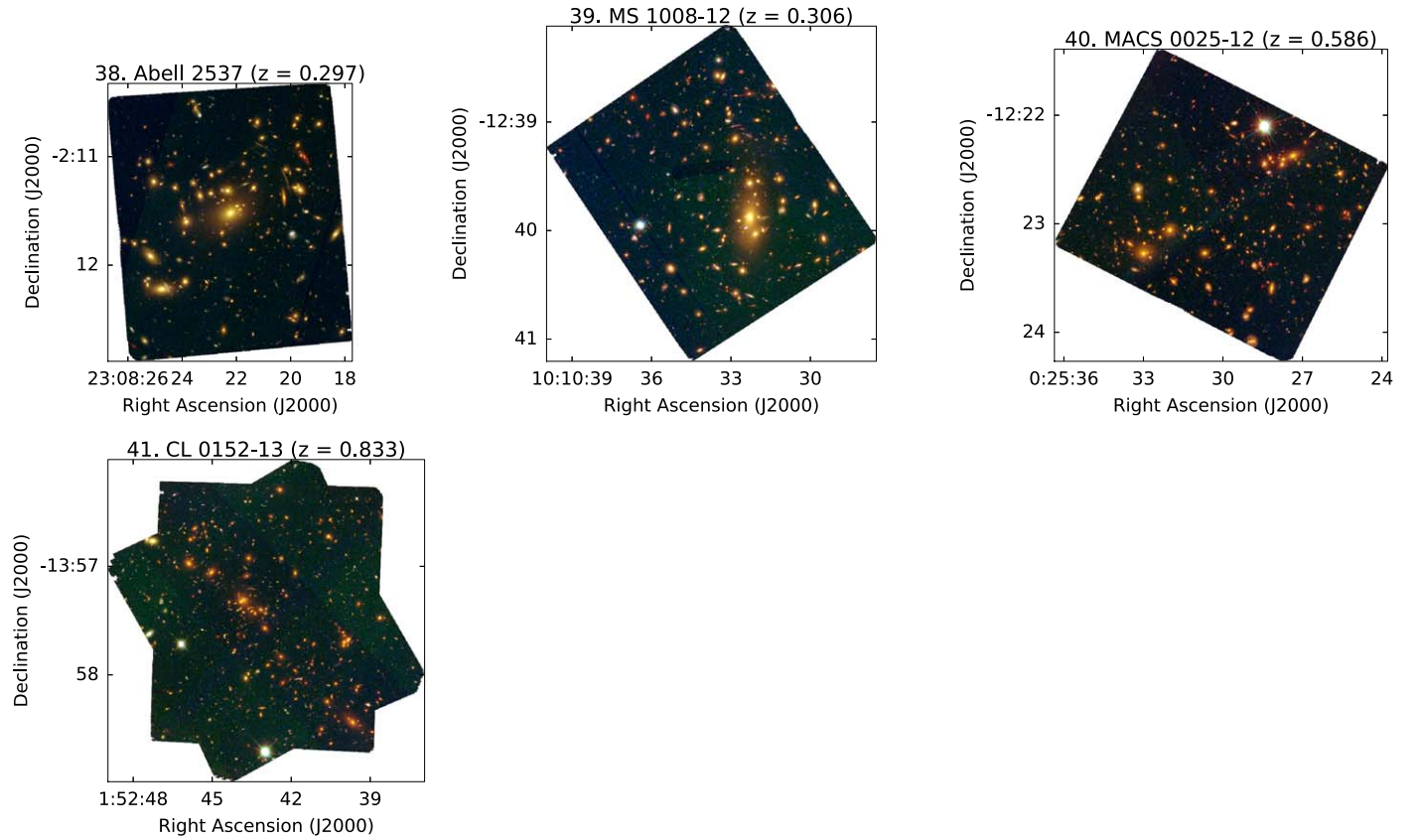


Figure 4. (Continued.)

Table 12
SExtractor Parameters Used in the RELICS *HST* Source Catalogs

SExtractor Parameter	acs-wfc3	wfc3ir	Description
DETECT_MINAREA	9	9	Contiguous pixels required above detection threshold
DETECT_THRESH	1	1	Detection threshold (σ above background rms)
BACK_SIZE	128	64	Background cell size
BACK_FILTERSIZE	5	3	Background grid size
DEBLEND_NTHRESH	32	64	Number of threshold levels
DEBLEND_MINCONT	0.0015	0.0001	Minimum contrast ratio
BACKPHOTO_TYPE	LOCAL	LOCAL	Method for measuring background
BACKPHOTO_THICK	24	24	Width of rectangular annulus around each object

As a caution to users, we note that the source catalogs include image artifacts such as diffraction spikes and objects poorly segmented by SExtractor. Additionally, photometry is complicated in crowded fields, especially as brighter cluster members contaminate the light from fainter, more distant objects.

5.3. Photometric Redshifts

Based on the *HST* photometry, we measured photometric redshifts using Bayesian Photometric Redshifts (BPZ; Benítez 2000; Coe et al. 2006) and Easy and Accurate z_{phot} from Yale (EAZY; Brammer et al. 2008), which were two of the top performing methods in controlled tests (Hildebrandt et al. 2010).

For BPZ, we used 11 spectral models shown in Figure 5 and described in Coe et al. (2013), Benítez et al. (2014), and Rafelski et al. (2015). Briefly, the model spectral energy

Table 13
Galactic Reddening Extinction Correction Coefficients A_λ for Each Filter

Camera	Filter	Coefficient
WFC3/UVIS	F390W	4.514
ACS	F435W	4.117
ACS	F475W	3.747
ACS	F555W	3.242
ACS, WFC3/UVIS	F606W	2.929
ACS	F625W	2.671
ACS	F775W	2.018
ACS	F814W	1.847
ACS	F850LP	1.473
WFC3/IR	F105W	1.015
WFC3/IR	F110W	0.876
WFC3/IR	F125W	0.757
WFC3/IR	F140W	0.609
WFC3/IR	F160W	0.470

Table 14
HST Source Catalog Content

Column	Parameter	Description
1	id	Object ID number
2	R.A.	Right ascension in decimal degrees (J2000)
3	Decl.	Declination in decimal degrees (J2000)
4	x	x pixel coordinate
5	y	y pixel coordinate
6	fwhm	Full width at half maximum (arcsec)
7	area	Isophotal aperture area (pixels)
8	stel	SExtractor “stellarity” (1 = star; 0 = galaxy)
9	ell	Ellipticity = $1 - B/A$
10	theta	Position angle (CCW wrt x axis; degrees)
11	nf5sig	Number of filters with a 5σ detection
12	nfobs	Number of filters observed for this object (in the field of view and without bad pixels)
13	f435w_mag	F435W isophotal magnitude (99 = non-detection; -99 = unobserved)
14	f435w_magerr	F435W isophotal magnitude uncertainty (or 1σ upper limit for nondetection)
15	f435w_flux	F435W isophotal flux ($e^- s^{-1}$)
16	f435w_fluxerr	F435W isophotal flux uncertainty ($e^- s^{-1}$)
17	f435w_fluxnJy	F435W isophotal flux (nJy)
18	f435w_fluxnJyerr	F435W isophotal flux uncertainty (nJy)
19	f435w_sig	F435W detection significance
...	...	(photometry in other filters)
62 ^a	bright_mag	Brightest magnitude in any filter
63	bright_magerr	Brightest magnitude uncertainty
64	zb	BPZ most likely Bayesian photometric redshift
65	zbmin	BPZ lower limit (95% confidence)
66	zbmax	BPZ upper limit (95% confidence)
67	tb	BPZ most likely spectral type (1–5 elliptical; 6–7 spiral; 8–11 starburst)
68	odds	$P(z)$ contained within $zb \pm 0.04(1+z)$
69	chisq	χ^2 poorness of BPZ fit: observed versus - model fluxes
70	chisq2	Modified χ^2 : model fluxes allowed uncertainties (Coe et al. 2006)
71	M0	Magnitude used as BPZ prior: F775W or closest available filter
72	zml	Maximum likelihood (flat prior) most likely redshift
73	tml	Maximum likelihood (flat prior) most likely spectral type

Note.

^a Column numbers will vary depending on the number of *HST* filters observed in each field.

distributions (SEDs) are originally from PEGASE (Fioc & Rocca-Volmerange 1997) but recalibrated, based on observed photometry and spectroscopic redshifts from FIREWORKS (Wuyts et al. 2008). The templates were selected to encompass ranges of metallicities, extinctions, and star formation histories observed for the vast majority of real galaxies. We allowed BPZ to interpolate nine templates between each pair of adjacent templates, yielding 101 templates altogether. BPZ fit the photometry to a grid of these 101 templates and 1300 redshifts linearly spaced from $z = 0.001$ to $z = 13$. BPZ tempers those χ^2 results with a Bayesian prior $P(z, T|m)$, which gives the likelihood of a redshift z and template type T given an observed magnitude m in F814W. We used the original BPZ prior derived from the HDFN (Benítez 2000) and plotted in Figure 6 for $m = 24$, 26, and ≥ 32 , the latter including F814W

nondetections. We do not attempt to correct magnitudes for lensing magnifications in our initial catalogs because those estimates are not available from the start. We note that our prior’s dependence on magnitude is often gradual, but magnification should be accounted for in a more accurate $P(z)$ estimate.

We used EAZY (Brammer et al. 2008) to obtain a second independent set of photometric redshift estimates. EAZY uses a different template set and allows interpolation between any pair of templates. The nine templates used here include seven from PEGASE, one very dusty and quiescent galaxy from Maraston (2005), and one extreme emission line galaxy (EELG) from Erb et al. (2010). We used a flat prior with EAZY, as we found that the default prior was systematically biased against high-redshift galaxies, strongly preferring lower-redshift EELGs with worse fits to the photometry (see discussion in Salmon et al. 2017).

Salmon et al. (2017) present a comparison of the templates and results from BPZ and EAZY for RELICS high- z candidates.

5.4. Spitzer Image Reductions

We reduced the *Spitzer* images using MOPEX (Makovoz & Khan 2005) and generated catalogs using T-PHOT (Merlin et al. 2015). The reduced images are available via IRSA. Currently these include data from programs 12005 and 12123 (totaling 5 hr of depth per filter). Deeper data from the additional three *Spitzer* programs (Table 10) will be included in future releases of reduced images. More details will be presented by V. Strait et al. (2019, in preparation). Due to the broader *Spitzer* PSF, extra care is required in obtaining aperture-matched *HST* + *Spitzer* photometry. Less careful *Spitzer* photometry can result in less accurate photometric redshifts (Hildebrandt et al. 2010). We did not use the *Spitzer* photometry in our initial photometric redshift catalog release. We did use the *Spitzer* photometry to vet our $z \sim 10$ candidates, and we will use it to study the properties of all our high-redshift candidates.

6. Results

To date, RELICS has delivered the following science results on high-redshift galaxies (Section 2.1), strong-lens modeling (Section 2.2), and SNe (Section 2.5). Reduced images, catalogs, and lens models are available via MAST and IRSA. Constraints on cluster masses (Section 2.3) and the dark matter particle cross section (Section 2.4) require weak-lensing data and analyses on a longer timescale.

6.1. High-redshift Candidates

RELICS yielded over 300 high-redshift candidates at $z \sim 6$ –8, including the brightest known at $z \sim 6$ (Salmon et al. 2017). These galaxies are lensed as brightly as F160W $H \sim 23$, enabling detailed studies of galaxy properties in the first billion years. Follow-up study is beginning to match some of these candidates as multiple images (Acebron et al. 2018) and deliver spectroscopic confirmations (Cibirka et al. 2018). We are following up RELICS high-redshift candidates with ground-based telescopes and instruments, including Keck/MOSFIRE, VLT/MUSE, Gemini/GMOS, Gemini-S/Flamingos-2, ALMA, and NOEMA/PdBI.

Table 15
HST Source Catalog: Detection and Shape Measurement

ID	α_{J2000} (deg)	δ_{J2000} (deg)	x (pixels)	y (pixels)	FWHM (arcsec)	Area (pixels)	Stellarity	Ellipticity (1 - b/a)	θ (deg)	$N_{f,5\sigma}$	$N_{f,obs}$
1	130.7320691	36.3412393	3212.886	1118.780	0.356	13	0.35	0.26	11.0	1	7
2	130.7567476	36.3856742	2020.442	3784.849	0.320	474	0.03	0.09	-42.8	7	7
3	130.7567488	36.3851756	2020.382	3754.932	0.754	125	0.00	0.33	58.4	7	7
4	130.7545731	36.3848770	2125.475	3737.004	0.173	42	0.98	0.06	-10.0	5	7
5	130.7535624	36.3842826	2174.292	3701.339	0.378	59	0.01	0.21	80.2	7	7

Note. Complete RELICS *HST* catalogs are available on MAST, including all parameters described in Table 14. This sample of the content is from the A697 IR-detection catalog.

Table 16
HST Source Catalog: Photometry in Each Filter

Magnitude (AB)	Flux ($e^- s^{-1}$)	Flux (nJy)	S/N
28.4629 \pm 0.4579	0.0760 \pm 0.0399	14.9573 \pm 7.8473	1.9100
24.2190 \pm 0.0567	3.7868 \pm 0.2031	745.4248 \pm 39.9764	18.6500
25.5322 \pm 0.1058	1.1298 \pm 0.1156	222.3921 \pm 22.7527	9.7700
99.0000 \pm 28.6848	-0.1387 \pm 0.0619	-27.3093 \pm 12.1918	-2.2400
25.6583 \pm 0.0796	1.0059 \pm 0.0765	198.0041 \pm 15.0577	13.1500

Note. Continuation of sample provided in Table 15. Parameters are described in Table 14. The photometry given here is from the F435W filter. In the full catalog, all filters are provided, followed by the brightest magnitude in any filter for reference.

RELICS also delivered SPT0615-JD, the most distant lensed arc known (Salmon et al. 2018). At $z \sim 10$ and spanning a full $2''.5$ on the sky, SPT0615-JD provides by far the most detailed view we have of any galaxy in the first 500 million years. (The two known $z \sim 11$ galaxies are not spatially resolved, despite lensing magnification in the case of MACS0647-JD from Coe et al. 2013 and the relatively high intrinsic luminosity of GN-z11 from Oesch et al. 2016.) ALMA observations have been awarded (PI Tamura) to search for the [O III] $88 \mu m$ line in the $z \sim 10$ lensed arc, continuing the success of that research group at $z \sim 7-9$ as noted in Section 2.1 (Inoue et al. 2016; Hashimoto et al. 2018; Tamura et al. 2019). An [O III] detection would yield the highest spectroscopic redshift confirmation to date, along with the earliest detection of heavy elements (oxygen).

RELICS *Spitzer* (SRELICS) imaging was crucial in distinguishing between bonafide $z \sim 10$ candidates and $z \sim 2$ interlopers. Salmon et al. (2018) actually identified three $z \sim 10$ candidates based on our *HST* imaging, but two turned out to be $z \sim 2$ interlopers based on the *Spitzer* photometry. Red $z \sim 2$ galaxies are significantly brighter at $3-5 \mu m$ than bluer $z \sim 10$ galaxies. RELICS *Spitzer* imaging will also enable us to measure stellar masses for our >300 candidates at $z \sim 6-8$.

Improved constraints on the $z \sim 9$ luminosity function from RELICS will require adding simulating lensed galaxies to our images to quantify our detection efficiency as a function of magnitude, position, and redshift (e.g., Livermore et al. 2017; Carrasco et al. 2018). But based on our current lack of any strong $z \sim 9$ candidates and a single $z \sim 10$ candidate (Salmon et al. 2017, 2018), our yields appear lower than expected at these redshifts, which may support the accelerated evolution scenario. Alternatively, more detailed study may shed light on

why we have missed galaxies at these redshifts in our searches and photometric redshift analyses.

At lower redshifts, RELICS is studying compact, low-metallicity dwarf galaxies that are excellent analogs to high-redshift galaxies but can be studied in greater detail. Analysis of one RELICS $z = 1.645$ galaxy shows that low-metallicity stars are driving C III] emission with the strongest rest-frame EW ($\sim 20 \text{ \AA}$) yet observed at these redshifts, suggesting a more intense radiation field than assumed by most population synthesis models (Mainali et al. 2019).

6.2. Lens Modeling

Strong-lens models of RELICS clusters are primarily used to estimate magnifications of our lensed galaxies and to correct the surveyed volume for lensing magnification (Section 2.2). We use three lens modeling methods, all of which assume that the observed cluster light traces some component of the cluster mass distribution: Lenstool (Kneib et al. 1996; Jullo & Kneib 2009; Johnson et al. 2014); Zitrin LTM, or light-traces-mass (Zitrin et al. 2009, 2015b); and GLAFIC (Oguri 2010). The use of multiple methods on an individual cluster yields a more accurate estimate of systematic uncertainties than using one method alone, as shown in analyses of Frontier Fields clusters (Coe et al. 2015; Acebron et al. 2017; Livermore et al. 2017; Remolina González et al. 2018).

RELICS has published strong-lens modeling analyses of 14 clusters to date (Acebron et al. 2018, 2019; Cerny et al. 2018; Cibirka et al. 2018; Paterno-Mahler et al. 2018; Mahler et al. 2019). These models are based on the multiband *HST* imaging and spectroscopic redshifts of strongly lensed galaxies obtained by our group and others. Most of these analyses have revealed lensing strengths on par with Frontier Fields clusters, quantified in terms of cumulative area with magnification greater than some threshold. Strong-lens models are currently available on MAST for 28/41 RELICS clusters, with the rest to be delivered in time for the *JWST* GO call for proposals. Our data products include maps of cluster mass, as well as lensing deflection, shear, and magnification.

Paterno-Mahler et al. (2018) used all three methods (primarily Lenstool) to model SPT0615-57 and study the $z \sim 10$ candidate discovered by Salmon et al. (2018). They delivered magnification estimates and explained the current lack of observed counterimages. Acebron et al. (2019) compared magnification estimates from two methods (Zitrin LTM and Lenstool) for the many (24) $z \sim 6-7$ candidates lensed by CL0152-13. Acebron et al. (2018) modeled two clusters with the Zitrin LTM method, including MACS0308+26, which lenses one of the brightest $z \sim 6$ candidates known. This paper identified two multiple images of that

Table 17
HST Source Catalog: Photometric Redshifts

z_{BPZ}	z_{min}	z_{max}	t_{BPZ}	ODDS	χ^2	χ^2_{mod}	M_0	z_{ML}	t_{ML}
2.741	0.225	3.470	9.5	0.148	0.940	1.334	28.102	2.730	9.5
0.222	0.145	0.255	4.1	0.850	0.933	0.158	22.015	0.190	4.2
1.033	0.631	1.115	9.6	0.481	0.163	0.212	25.013	1.040	9.6
4.501	4.315	4.698	8.2	0.974	1.292	1.367	25.835	4.520	8.2
0.778	0.461	0.961	10.3	0.473	0.112	0.770	25.346	0.780	10.2

Note. Continuation of sample provided in Table 15. Parameters are described in Table 14.

Table 18
RELICS Supernovae and HST Follow-up Imaging

Cluster	Supernova ^a	Abbreviation ^b	R.A. (J2000)	Decl. (J2000)	Notes
rxo0949+17	Eleanor ^c	RLC11Ele	09:49:47.97	+17:07:24.9	cluster member
rxo0949+17	Alexander ^c	RLC11Ale	09:49:48.07	+17:07:24.0	cluster member
rxo0949+17	Antikythera	RLC15Ant	09:49:48.01	+17:07:23.0	cluster member
rxo0142+44	Makapansgat	RLC16Mak	01:43:16.326	+44:33:50.65	parallel field
abell1763	Nebra	RLC16Neb	13:35:15.13	+41:00:15.8	lensed
macs0025-12	Quipu	RLC16Qui	00:25:31.977	-12:23:31.80	cluster member
macs0257-23	Cheomseongdae	RLC16Che	02:57:07.795	-23:27:11.69	lensed or cluster member
plckg171-40	Kukulkan	RLC16Kuk	03:12:59.148	+08:22:43.60	cluster member
clj0152-13	Nimrud	RLC16Nim	01:52:40.352	-13:57:44.81	lensed
rxo0600-20	William	RLC17Wil	06:00:12.227	-20:07:23.91	cluster member
smacs0723-73	Yupana	RLC17Yup	07:23:28.40	-73:27:03.6	lensed or cluster member

Notes.

^a Each SN was named after a historical relic, with the exceptions of Eleanor and Alexander, named after Deputy PI Bradley's children, and William, named after PI Coe's newborn son.

^b Abbreviations include the last two digits of the year of appearance.

^c Discovered in pre-RELICS imaging based on difference comparison with RELICS imaging.

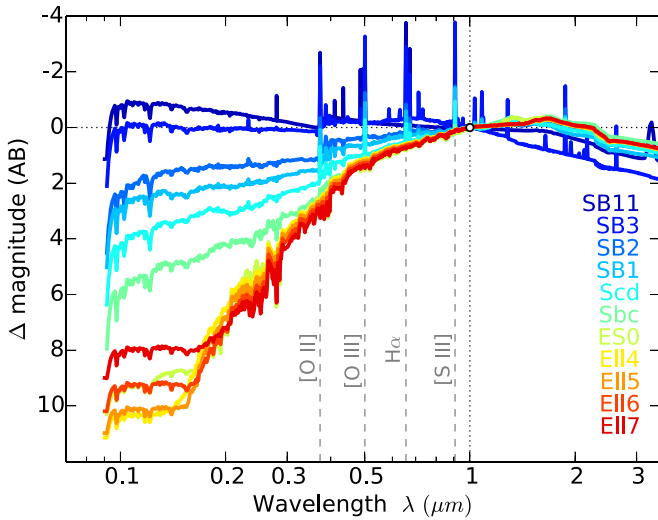


Figure 5. The 11 BPZ template SEDs used in this work, consisting of four elliptical galaxies (EII), one lenticular (ES0), and four starbursts (SB). These templates are based on PEGASE (Fioc & Rocca-Volmerange 1997) but recalibrated based on observed photometry and spectroscopic redshifts from FIREWORKS (Wuyts et al. 2008). The starbursts and Scd spiral contain emission lines, four of which are labeled in gray. All spectra are normalized to the same magnitude at 1 μm .

galaxy lensed to $J \sim 23.2$ and 24.6 AB. Mahler et al. (2019) used spectroscopic redshifts of many arcs from VLT/MUSE (Jauzac et al. 2019) to produce a detailed Lenstool model of MACS0417-11, confirming that it is a strong lens, despite

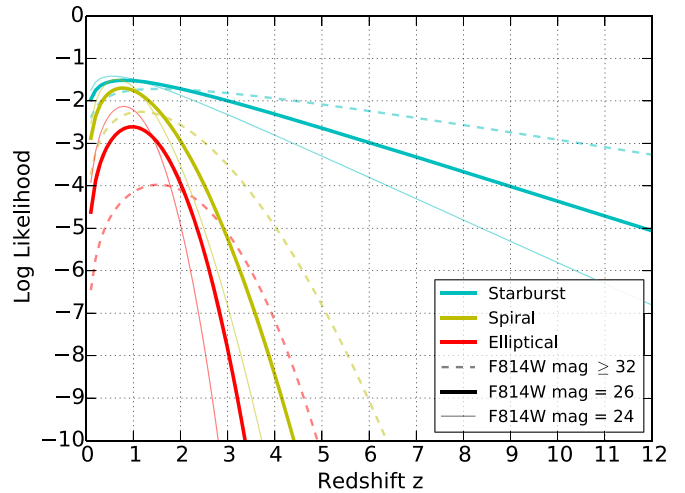


Figure 6. For BPZ, we use the Bayesian redshift prior derived from the HDFN (Benítez 2000). Here we show priors for galaxies of different spectral types and with F814W AB magnitudes of 24, 26, and ≥ 32 , including nondetections.

curiously yielding no $z \sim 6-8$ candidates (Salmon et al. 2017). Cibirka et al. (2018) modeled four clusters using the LTM method and presented one lensed galaxy showing strong Ly α emission with a spectroscopic redshift $z = 5.800$. Cerny et al. (2018) modeled five clusters using Lenstool and presented detailed estimates of the statistical and systematic uncertainties. They present new spectroscopic redshifts and a new method to mitigate modeling uncertainties due to photometric redshifts.

Wide-field imaging for weak-lensing analyses from Subaru and Magellan is in hand for many RELICS clusters, as are X-ray data from *Chandra* and *XMM-Newton*, along with *Planck* SZ mass measurements. Combining these with strong-lensing mass measurements from *HST* will improve both precision and accuracy on the overall mass calibration of massive clusters (Section 2.3) and contribute to constraints on the dark matter particle cross section (Section 2.4).

6.3. Supernovae

The RELICS observing strategy (Section 2.5) yielded 11 SNe, summarized here for the first time in Table 18. Most of these are cluster members, as expected. The first three SNe, all found in the RXC 0949+17 cluster, were announced in Rodney et al. (2015a). Three of the other RELICS SNe are lensed, and we obtained follow-up *HST* imaging of them, using 20 orbits allocated to RELICS for this purpose (Table 7). The most distant, dubbed “Nebra,” is a $z \sim 2$ candidate Type Ia lensed by A1763 (Rodney et al. 2016a). If the redshift and type were confirmed, Nebra would be among the most distant SNe Ia known. The current record holder at $z = 2.22$ is also lensed (Rubin et al. 2018).

7. Summary

With RELICS observations complete, the 34 most massive *Planck* clusters ($M_{500} > 8.8 \times 10^{14} M_{\odot}$) now all have *HST* optical and near-infrared imaging, as well as *Spitzer* infrared imaging. Based on this imaging, we have discovered over 300 $z \sim 6$ –10 candidates, including the brightest galaxies known at $z \sim 6$ (Salmon et al. 2017) and the most distant spatially resolved lensed arc known, SPT0615-JD at $z \sim 10$ (Salmon et al. 2018). These are among the best and brightest targets for detailed follow-up study from the first billion years after the big bang. Follow-up observations of RELICS fields are currently being carried out with facilities including Keck, VLT, Subaru, Magellan, MMT, GMRT, and ALMA.

At lower redshifts, RELICS is studying compact, low-metallicity dwarf galaxies that are excellent analogs to high-redshift galaxies but can be studied in greater detail. We have also discovered 11 SNe (Table 18).

To date, we have published strong-lens modeling analyses of 14 RELICS clusters (Acebron et al. 2018, 2019; Cerny et al. 2018; Cibirka et al. 2018; Paterno-Mahler et al. 2018; Mahler et al. 2019). Many of the clusters modeled so far have proven to be comparable to the strongest lenses known. By combining our strong-lensing analyses of the cluster cores with weak-lensing analyses from ground-based imaging covering the full clusters out to their virial radii, we can derive robust mass profiles for these clusters. Our cluster mass measurements will help inform SZ mass scaling relations.

RELICS has proven once again that cluster lensing delivers distant galaxies more efficiently than blank-field observations. The efficiency gains are greatest for discoveries of relatively bright galaxies. We expect these gains to be even greater at higher redshifts. Our lens modeling analyses of RELICS clusters will identify which cluster lenses are truly among the best to use going forward to efficiently search for the first galaxies.

RELICS *HST* reduced images, catalogs, and lens models are available via MAST at doi:10.17909/T9SP45. RELICS *Spitzer* reduced images are available via IRSA.

We thank Lindsey Bleem for providing Magellan Megacam LDSS3 images of SPT0254-58 and AS295 prior to RELICS to inform our *HST* observations of these clusters. We thank Florian Pacaud and Matthias Klein for discussions regarding our AS295 *HST* pointings. We thank Dale Kocevski for an image of RXC 0142+44 obtained with the University of Hawaii 2.2 m telescope. And we thank Stella Seitz et al. for sharing their *HST* observations of PLCK G287+32 obtained during the same cycle.

We thank the STScI and SSC directors and time allocation committees for enabling these large observing programs. We are grateful to our *HST* program coordinator William Januszewski for implementing the RELICS *HST* observations. We thank Jennifer Mack for expert mentoring of our *HST* image reduction gurus RA and SO. And we thank Gabriel Brammer for providing an updated WFC3/IR hot pixel mask derived from science observations from GO 14114.

We are grateful to the University of Arizona for hosting our team meeting.

The RELICS Hubble Treasury Program (GO 14096) consists of observations obtained by the NASA/ESA *Hubble Space Telescope* (*HST*). *HST* is operated by the Association of Universities for Research in Astronomy, Inc. (AURA), under NASA contract NAS5-26555.

Data from the NASA/ESA *HST* presented in this paper were obtained from the Mikulski Archive for Space Telescopes (MAST), operated by the Space Telescope Science Institute (STScI). STScI is operated by the Association of Universities for Research in Astronomy, Inc. (AURA), under NASA contract NAS 5-26555. The *HST* Advanced Camera for Surveys (ACS) was developed under NASA contract NAS 5-32864.

Spitzer Space Telescope data presented in this paper were obtained from the NASA/IPAC Infrared Science Archive (IRSA), operated by the Jet Propulsion Laboratory, California Institute of Technology. *Spitzer* and IRSA are operated by the Jet Propulsion Laboratory, California Institute of Technology, under contract with NASA.

We gratefully acknowledge support from JPL for the *Spitzer* analysis. M.B. and V.S. also acknowledge support by NASA through ADAP grant 80NSSC18K0945, NASA/*HST* through HST-GO-14096, HST-GO-13666, and two awards issued by *Spitzer*/JPL/Caltech associated with the SRELICS_DEEP and SRELICS programs.

Part of this work by W.D. was performed under the auspices of the U.S. DOE by LLNL under contract DE-AC52-07NA27344. K.U. acknowledges support from the Ministry of Science and Technology of Taiwan (grant MOST 106-2628-M-001-003-MY3) and from Academia Sinica (grant AS-IA-107-M01). O.G. is supported by an NSF Astronomy and Astrophysics Fellowship under award AST-1602595. S.A.R. was supported by NASA grant HST-GO-14208 from STScI, which is operated by Associated Universities for Research in Astronomy, Inc. (AURA), under NASA contract NAS 5-26555. A.M. acknowledges the financial support of the Brazilian funding agency FAPESP (Post-doc fellowship—process No. 2014/11806-9). J.H. was supported by a VILLUM FONDEN Investigator grant (project No. 16599).

Finally, we thank our referee for detailed comments that helped us improve the manuscript.

Facilities: *HST* (WFC3, ACS); *Spitzer* (IRAC); *Planck*; MAST; IRSA.

ORCID iDs

Dan Coe  <https://orcid.org/0000-0001-7410-7669>
 Brett Salmon  <https://orcid.org/0000-0002-7453-7279>
 Maruša Bradač  <https://orcid.org/0000-0001-5984-0395>
 Larry D. Bradley  <https://orcid.org/0000-0002-7908-9284>
 Keren Sharon  <https://orcid.org/0000-0002-7559-0864>
 Adi Zitrin  <https://orcid.org/0000-0002-0350-4488>
 Ana Acebron  <https://orcid.org/0000-0003-3108-9039>
 Nathália Cibirka  <https://orcid.org/0000-0002-2356-4680>
 Victoria Strait  <https://orcid.org/0000-0002-6338-7295>
 Rachel Paterno-Mahler  <https://orcid.org/0000-0003-3653-3741>
 Guillaume Mahler  <https://orcid.org/0000-0003-3266-2001>
 Kuang-Han Huang  <https://orcid.org/0000-0001-7826-6448>
 Ramesh Mainali  <https://orcid.org/0000-0003-0094-6827>
 Pascal A. Oesch  <https://orcid.org/0000-0001-5851-6649>
 Michele Trenti  <https://orcid.org/0000-0001-9391-305X>
 Daniela Carrasco  <https://orcid.org/0000-0002-3772-0330>
 William A. Dawson  <https://orcid.org/0000-0003-0248-6123>
 Steven A. Rodney  <https://orcid.org/0000-0003-1947-687X>
 Keiichi Umetsu  <https://orcid.org/0000-0002-7196-4822>
 Benedetta Vulcani  <https://orcid.org/0000-0003-0980-1499>
 Or Graur  <https://orcid.org/0000-0002-4391-6137>
 Saurabh W. Jha  <https://orcid.org/0000-0001-8738-6011>
 Melissa L. Graham  <https://orcid.org/0000-0002-9154-3136>
 Jens Hjorth  <https://orcid.org/0000-0002-4571-2306>
 Jonatan Selsing  <https://orcid.org/0000-0001-9058-3892>
 Lise Christensen  <https://orcid.org/0000-0001-8415-7547>
 Shotaro Kikuchiara  <https://orcid.org/0000-0003-2449-6314>
 Masami Ouchi  <https://orcid.org/0000-0002-1049-6658>
 Masamune Oguri  <https://orcid.org/0000-0003-3484-399X>
 Felipe Andrade-Santos  <https://orcid.org/0000-0002-8144-9285>
 Austin T. Hoag  <https://orcid.org/0000-0001-8989-2567>
 Traci L. Johnson  <https://orcid.org/0000-0002-8829-5303>
 Rachael Livermore  <https://orcid.org/0000-0003-4456-1566>
 Daniel Lam  <https://orcid.org/0000-0002-6536-5575>
 Sune Toft  <https://orcid.org/0000-0003-3631-7176>

References

- Abell, G. O. 1958, *ApJS*, **3**, 211
 Abell, G. O., Corwin, H. G., Jr., & Olowin, R. P. 1989, *ApJS*, **70**, 1
 Acebron, A., Alon, M., Zitrin, A., et al. 2019, *ApJ*, **874**, 132
 Acebron, A., Cibirka, N., Zitrin, A., et al. 2018, *ApJ*, **858**, 42
 Acebron, A., Jullo, E., Limousin, M., et al. 2017, *MNRAS*, **470**, 1809
 Albert, J. G., Sifón, C., Stroe, A., et al. 2017, *A&A*, **607**, A4
 Applegate, D. E., von der Linden, A., Kelly, P. L., et al. 2014, *MNRAS*, **439**, 48
 Atek, H., Richard, J., Kneib, J.-P., & Schaerer, D. 2018, *MNRAS*, **479**, 5184
 Battaglia, N., Leauthaud, A., Miyatake, H., et al. 2016, *JCAP*, **2016**, 013
 Benítez, N. 2000, *ApJ*, **536**, 571
 Benítez, N., Dupke, R., Moles, M., et al. 2014, arXiv:1403.5237
 Bertin, E., & Arnouts, S. 1996, *A&AS*, **117**, 393
 Bleem, L. E., Stalder, B., de Haan, T., et al. 2015, *ApJS*, **216**, 27
 Bosch-Ramon, V. 2018, *A&A*, **617**, L3
 Bouwens, R. J., Bradley, L., Zitrin, A., et al. 2014, *ApJ*, **795**, 126
 Bouwens, R. J., Illingworth, G. D., Oesch, P. A., et al. 2012, *ApJ*, **754**, 83
 Bouwens, R. J., Illingworth, G. D., Oesch, P. A., et al. 2015, *ApJ*, **803**, 34
 Bradač, M., Allen, S. W., Treu, T., et al. 2008, *ApJ*, **687**, 959
 Bradač, M., Clowe, D., Gonzalez, A. H., et al. 2006, *ApJ*, **652**, 937
 Bradač, M., Ryan, R., Casertano, S., et al. 2014, *ApJ*, **785**, 108
 Bradač, M., Vanzella, E., Hall, N., et al. 2012, *ApJL*, **755**, L7
 Bradley, L. D., Bouwens, R. J., Ford, H. C., et al. 2008, *ApJ*, **678**, 647
 Bradley, L. D., Trenti, M., Oesch, P. A., et al. 2012, *ApJ*, **760**, 108
 Bradley, L. D., Zitrin, A., Coe, D., et al. 2014, *ApJ*, **792**, 76
 Brammer, G. B., Pirzkal, N., McCullough, P., & MacKenty, J. W. 2014, WFC3 Instrument Science Rep. 2014-03, Tech. Rep., STScI
 Brammer, G. B., van Dokkum, P. G., & Coppi, P. 2008, *ApJ*, **686**, 1503
 Brauhar, J. R., Dale, D. A., & Helou, G. 2008, *ApJS*, **178**, 280
 Broadhurst, T. J., Taylor, A. N., & Peacock, J. A. 1995, *ApJ*, **438**, 49
 Calvi, V., Trenti, M., Stiavelli, M., et al. 2016, *ApJ*, **817**, 120
 Capak, P. L., Carilli, C., Jones, G., et al. 2015, *Natur*, **522**, 455
 Carniani, S., Maiolino, R., Amorin, R., et al. 2018, *MNRAS*, **478**, 1170
 Carniani, S., Maiolino, R., Pallottini, A., et al. 2017, *A&A*, **605**, A42
 Carrasco, D., Trenti, M., Mutch, S., & Oesch, P. A. 2018, *PASA*, **35**, e022
 Cerny, C., Sharon, K., Andrade-Santos, F., et al. 2018, *ApJ*, **859**, 159
 Chan, B. M. Y., Broadhurst, T., Lim, J., et al. 2017, *ApJ*, **835**, 44
 Chen, W., Kelly, P. L., Diego, J. M., et al. 2019, *ApJ*, **881**, 8
 Cibirka, N., Acebron, A., Zitrin, A., et al. 2018, *ApJ*, **863**, 145
 Clowe, D., Bradač, M., Gonzalez, A. H., et al. 2006, *ApJL*, **648**, L109
 Coe, D. 2010, arXiv:1005.0411
 Coe, D. 2018, *SciAm*, **319**, 40
 Coe, D., Benítez, N., Sánchez, S. F., et al. 2006, *AJ*, **132**, 926
 Coe, D., Bradley, L., & Zitrin, A. 2015, *ApJ*, **800**, 84
 Coe, D., Umetsu, K., Zitrin, A., et al. 2012, *ApJ*, **757**, 22
 Coe, D., Zitrin, A., Carrasco, M., et al. 2013, *ApJ*, **762**, 32
 Czakon, N. G., Sayers, J., Mantz, A., et al. 2015, *ApJ*, **806**, 18
 Dawson, W. A., Wittman, D., Jee, M. J., et al. 2012, *ApJL*, **747**, L42
 Dayal, P., & Ferrara, A. 2018, *PhR*, **780**, 1
 De Looze, I., Cormier, D., Leboutteiller, V., et al. 2014, *A&A*, **568**, A62
 Du, X., Shapley, A. E., Martin, C. L., & Coil, A. L. 2017, *ApJ*, **838**, 63
 Ebeling, H., Barrett, E., Donovan, D., et al. 2007, *ApJL*, **661**, L33
 Ebeling, H., Edge, A. C., Allen, S. W., et al. 2000a, *MNRAS*, **318**, 333
 Ebeling, H., Edge, A. C., Bohringer, H., et al. 1998, *MNRAS*, **301**, 881
 Ebeling, H., Edge, A. C., Burgett, W. S., et al. 2013, *MNRAS*, **432**, 62
 Ebeling, H., Edge, A. C., & Henry, J. P. 2001, *ApJ*, **553**, 668
 Ebeling, H., Edge, A. C., Mantz, A., et al. 2010, *MNRAS*, **407**, 83
 Ebeling, H., Jones, L. R., Perlman, E., et al. 2000b, *ApJ*, **534**, 133
 Erb, D. K., Pettini, M., Shapley, A. E., et al. 2010, *ApJ*, **719**, 1168
 Finkelstein, S. L. 2016, *PASA*, **33**, e037
 Finkelstein, S. L., D'Aloisio, A., Paardekoope, J.-P., et al. 2019, *ApJ*, **879**, 36
 Fioc, M., & Rocca-Volmerange, B. 1997, *A&A*, **326**, 950
 Franx, M., Illingworth, G. D., Kelson, D. D., van Dokkum, P. G., & Tran, K.-V. 1997, *ApJL*, **486**, L75
 Gioia, I. M., Maccacaro, T., Schild, R. E., et al. 1990, *ApJS*, **72**, 567
 Gonzaga, S., Hack, W., Fruchter, A., & Mack, J. 2012, The DrizzlePac Handbook (Baltimore, MD: STScI)
 Grandis, S., Mohr, J. J., Dietrich, J. P., et al. 2019, *MNRAS*, **488**, 2041
 Graur, O., Rodney, S. A., Maoz, D., et al. 2014, *ApJ*, **783**, 28
 Grillo, C., Rosati, P., Suyu, S. H., et al. 2018, *ApJ*, **860**, 94
 Grogin, N. A., Kocevski, D. D., Faber, S. M., et al. 2011, *ApJS*, **197**, 35
 Gruen, D., Seitz, S., Becker, M. R., Friedrich, O., & Mana, A. 2015, *MNRAS*, **449**, 4264
 Hamilton-Morris, V., Smith, G. P., Edge, A. C., et al. 2012, *ApJL*, **748**, L23
 Harikane, Y., Ouchi, M., Shibuya, T., et al. 2018, *ApJ*, **859**, 84
 Harvey, D., Massey, R., Kitching, T., Taylor, A., & Tittley, E. 2015, *Sci*, **347**, 1462
 Hashimoto, T., Inoue, A. K., Mawatari, K., et al. 2019, *PASJ*, **71**, 71
 Hashimoto, T., Laporte, N., Mawatari, K., et al. 2018, *Natur*, **557**, 392
 Hasselfield, M., Hilton, M., Marriage, T. A., et al. 2013, *JCAP*, **7**, 008
 Hildebrandt, H., Arnouts, S., Capak, P., et al. 2010, *A&A*, **523**, A31
 Hoag, A., Bradač, M., Huang, K.-H., et al. 2019, *ApJ*, **878**, 12
 Hoag, A., Bradač, M., Trenti, M., et al. 2017, *NatAs*, **1**, 0091
 Hoekstra, H., Herbonnet, R., Muzzin, A., et al. 2015, *MNRAS*, **449**, 685
 Hsu, L.-Y., Ebeling, H., & Richard, J. 2013, *MNRAS*, **429**, 833
 Huang, K.-H., Bradač, M., Lemaux, B. C., et al. 2016, *ApJ*, **817**, 11
 Infante, L., Zheng, W., Laporte, N., et al. 2015, *ApJ*, **815**, 18
 Inoue, A. K., Shimizu, I., Tamura, Y., et al. 2014, *ApJL*, **780**, L18
 Inoue, A. K., Tamura, Y., Matsuo, H., et al. 2016, *Sci*, **352**, 1559
 Ishigaki, M., Kawamata, R., Ouchi, M., et al. 2018, *ApJ*, **854**, 73
 Izotov, Y. I., Worsack, G., Schaerer, D., et al. 2018, *MNRAS*, **478**, 4851
 Jauzac, M., Mahler, G., Edge, A. C., et al. 2019, *MNRAS*, **483**, 3082
 Johnson, T. L., Rigby, J. R., Sharon, K., et al. 2017, *ApJL*, **843**, L21
 Johnson, T. L., & Sharon, K. 2016, *ApJ*, **832**, 82
 Johnson, T. L., Sharon, K., Bayliss, M. B., et al. 2014, *ApJ*, **797**, 48
 Jullo, E., & Kneib, J. 2009, *MNRAS*, **395**, 1319
 Kurov, A. A., Dai, L., Venumadhav, T., Miralda-Escudé, J., & Frye, B. 2019, *ApJ*, **880**, 58
 Kauch, W., Schindler, S., Erben, T., Wambsganss, J., & Schwoppe, A. 2010, *A&A*, **513**, A8
 Kawamata, R., Ishigaki, M., Shimasaku, K., et al. 2018, *ApJ*, **855**, 4
 Kelly, P. L., Diego, J. M., Rodney, S., et al. 2018, *NatAs*, **2**, 334
 Kelly, P. L., Rodney, S. A., Treu, T., et al. 2015, *Sci*, **347**, 1123
 Kelly, P. L., Rodney, S. A., & Treu, T. 2016, *ApJL*, **819**, L8

- Kneib, J.-P., Ellis, R. S., Smail, I., Couch, W. J., & Sharples, R. M. 1996, *ApJ*, **471**, 643
- Kneib, J.-P., & Natarajan, P. 2011, *A&ARv*, **19**, 47
- Kocevski, D. D., Ebeling, H., Mullis, C. R., & Tully, R. B. 2007, *ApJ*, **662**, 224
- Koekemoer, A. M., Faber, S. M., Ferguson, H. C., et al. 2011, *ApJS*, **197**, 36
- Koekemoer, A. M., Fruchter, A. S., Hook, R. N., & Hack, W. 2002, MultiDrizzle: An Integrated Pyraf Script for Registering, Cleaning and Combining Images, in The 2002 HST Calibration Workshop, ed. S. Arribas, A. Koekemoer, & B. Whitmore (Baltimore, MD: STSci), 337
- Laporte, N., Ellis, R. S., Boone, F., et al. 2017a, *ApJL*, **837**, L21
- Laporte, N., Nakajima, K., Ellis, R. S., et al. 2017b, *ApJ*, **851**, 40
- Le Fèvre, O., Lemaux, B. C., Nakajima, K., et al. 2019, *A&A*, **625**, 51
- Leitherer, C., Hernandez, S., Lee, J. C., & Oey, M. S. 2016, *ApJ*, **823**, 64
- Livermore, R. C., Finkelstein, S. L., & Lotz, J. M. 2017, *ApJ*, **835**, 113
- Lotz, J. M., Koekemoer, A., Coe, D., et al. 2017, *ApJ*, **837**, 97
- Madau, P. 2017, *ApJ*, **851**, 50
- Mahler, G., Sharon, K., Fox, C., et al. 2019, *ApJ*, **873**, 96
- Mainali, R., Kollmeier, J. A., Stark, D. P., et al. 2017, *ApJL*, **836**, L14
- Mainali, R., Stark, D. P., Tang, M., et al. 2019, *MNRAS*, submitted
- Mainali, R., Zitrin, A., Stark, D. P., et al. 2018, *MNRAS*, **479**, 1180
- Makovoz, D., & Khan, I. 2005, in ASP Conf. Ser. 347, Astronomical Data Analysis Software and Systems XIV, ed. P. Shopbell, M. Britton, & R. Ebert (San Francisco, CA: ASP), 81
- Malhotra, S., Helou, G., Stacey, G., et al. 1997, *ApJL*, **491**, L27
- Mann, A. W., & Ebeling, H. 2012, *MNRAS*, **420**, 2120
- Mantz, A., Allen, S. W., Ebeling, H., Rapetti, D., & Drlica-Wagner, A. 2010, *MNRAS*, **406**, 1773
- Maraston, C. 2005, *MNRAS*, **362**, 799
- Marrone, D. P., Spilker, J. S., Hayward, C. C., et al. 2018, *Natur*, **553**, 51
- Mason, C. A., Fontana, A., Treu, T., et al. 2019, *MNRAS*, **485**, 3947
- Mason, C. A., Treu, T., Dijkstra, M., et al. 2018, *ApJ*, **856**, 2
- McLeod, D. J., McLure, R. J., & Dunlop, J. S. 2016, *MNRAS*, **459**, 3812
- Medezinski, E., Battaglia, N., Umetsu, K., et al. 2018, *PASJ*, **70**, S28
- Meneghetti, M., Fedeli, C., Pace, F., Gottlöber, S., & Yepes, G. 2010, *A&A*, **519**, A90
- Meneghetti, M., Natarajan, P., Coe, D., et al. 2017, *MNRAS*, **472**, 3177
- Merlin, E., Fontana, A., Ferguson, H. C., et al. 2015, *A&A*, **582**, A15
- Molino, A., Benítez, N., Ascaso, B., et al. 2017, *MNRAS*, **470**, 95
- Morishita, T., Trenti, M., Stiavelli, M., et al. 2018, *ApJ*, **867**, 150
- Nagai, D., Vikhlinin, A., & Kravtsov, A. V. 2007, *ApJ*, **655**, 98
- Nakajima, K., Schaerer, D., Le Fèvre, O., et al. 2018, *A&A*, **612**, A94
- Nordin, J., Rubin, D., Richard, J., et al. 2014, *MNRAS*, **440**, 2742
- Oesch, P. A., Bouwens, R. J., Illingworth, G. D., et al. 2014, *ApJ*, **786**, 108
- Oesch, P. A., Bouwens, R. J., Illingworth, G. D., Labbé, I., & Stefanon, M. 2018, *ApJ*, **855**, 105
- Oesch, P. A., Brammer, G., van Dokkum, P. G., et al. 2016, *ApJ*, **819**, 129
- Oesch, P. A., van Dokkum, P. G., Illingworth, G. D., et al. 2015, *ApJL*, **804**, L30
- Oguri, M. 2010, *PASJ*, **62**, 1017
- Oke, J. B. 1974, *ApJS*, **27**, 21
- Oke, J. B., & Gunn, J. E. 1983, *ApJ*, **266**, 713
- Patel, B., McCully, C., Jha, S. W., et al. 2014, *ApJ*, **786**, 9
- Paterno-Mahler, R., Sharon, K., Coe, D., et al. 2018, *ApJ*, **863**, 154
- Penna-Lima, M., Bartlett, J. G., Rozo, E., et al. 2017, *A&A*, **604**, A89
- Piffaretti, R., Arnaud, M., Pratt, G. W., Pointecouteau, E., & Melin, J.-B. 2011, *A&A*, **534**, A109
- Pillepich, A., Reiprich, T. H., Porciani, C., Borm, K., & Merloni, A. 2018, *MNRAS*, **481**, 613
- Pirzkal, N., Coe, D., Frye, B. L., et al. 2015, *ApJ*, **804**, 11
- Planck Collaboration, Ade, P. A. R., Aghanim, N., et al. 2011, *A&A*, **536**, A11
- Planck Collaboration, Ade, P. A. R., Aghanim, N., et al. 2014, *A&A*, **571**, A29
- Planck Collaboration, Ade, P. A. R., Aghanim, N., et al. 2016a, *A&A*, **594**, A27
- Planck Collaboration, Ade, P. A. R., Aghanim, N., et al. 2016b, *A&A*, **594**, A13
- Planck Collaboration, Ade, P. A. R., Aghanim, N., et al. 2016c, *A&A*, **594**, A24
- Planck Collaboration, Ade, P. A. R., Aghanim, N., et al. 2016d, *A&A*, **586**, A139
- Planck Collaboration, Aghanim, N., & Akrami, Y. 2018a, arXiv:1807.06209
- Planck Collaboration, Aghanim, N., Ashdown, M., et al. 2016e, *A&A*, **596**, A107
- Planck Collaboration, Akrami, Y., Arroja, F., et al. 2018b, arXiv:1807.06205
- Postman, M., Coe, D., Benítez, N., et al. 2012, *ApJS*, **199**, 25
- Puschig, J., Hayes, M., Östlin, G., et al. 2017, *MNRAS*, **469**, 3252
- Rafelski, M., Teplitz, H. I., Gardner, J. P., et al. 2015, *AJ*, **150**, 31
- Randall, S. W., Markevitch, M., Clowe, D., Gonzalez, A. H., & Bradač, M. 2008, *ApJ*, **679**, 1173
- Rasia, E., Meneghetti, M., Martino, R., et al. 2012, *NJPh*, **14**, 055018
- Remolina González, J. D., Sharon, K., & Mahler, G. 2018, *ApJ*, **863**, 60
- Repp, A., & Ebeling, H. 2018, *MNRAS*, **479**, 844
- Repp, A., Ebeling, H., & Richard, J. 2016, *MNRAS*, **457**, 1399
- Rigby, J. R., Bayliss, M. B., Gladders, M. D., et al. 2015, *ApJL*, **814**, L6
- Rivera-Thorsen, T. E., Dahle, H., Gronke, M., et al. 2017, *A&A*, **608**, L4
- Roberts-Borsani, G. W., Bouwens, R. J., Oesch, P. A., et al. 2016, *ApJ*, **823**, 143
- Robertson, A., Harvey, D., Massey, R., et al. 2019, *MNRAS*, **488**, 3646
- Robertson, B. E., Ellis, R. S., Furlanetto, S. R., & Dunlop, J. S. 2015, *ApJL*, **802**, L19
- Rodney, S., Bradley, L., Coe, D., et al. 2015a, ATel, **8170**, 1
- Rodney, S., Coe, D., Bradley, L., et al. 2016a, ATel, **9224**, 1
- Rodney, S. A., Balestra, I., Bradac, M., et al. 2018, *NatAs*, **2**, 324
- Rodney, S. A., Patel, B., Scolnic, D., et al. 2015b, *ApJ*, **811**, 70
- Rodney, S. A., Riess, A. G., Strolger, L.-G., et al. 2014, *AJ*, **148**, 13
- Rodney, S. A., Strolger, L. G., Kelly, P. L., et al. 2016b, *ApJ*, **820**, 50
- Rubin, D., Hayden, B., Huang, X., et al. 2018, *ApJ*, **866**, 65
- Ryan, R. E., Jr., Gonzalez, A. H., Lemaux, B. C., et al. 2014, *ApJL*, **786**, L4
- Salmon, B., Coe, D., Bradley, L., et al. 2017, arXiv:1710.08930
- Salmon, B., Coe, D., Bradley, L., et al. 2018, *ApJL*, **864**, L22
- Schenker, M. A., Ellis, R. S., Konidaris, N. P., & Stark, D. P. 2014, *ApJ*, **795**, 20
- Schlafly, E. F., & Finkbeiner, D. P. 2011, *ApJ*, **737**, 103
- Schlegel, D. J., Finkbeiner, D. P., & Davis, M. 1998, *ApJ*, **500**, 525
- Schmidt, K. B., Huang, K.-H., Treu, T., et al. 2017, *ApJ*, **839**, 17
- Schmidt, K. B., Treu, T., Bradač, M., et al. 2016, *ApJ*, **818**, 38
- Senchyna, P., Stark, D. P., Vidal-García, A., et al. 2017, *MNRAS*, **472**, 2608
- Sereno, M. 2015, *MNRAS*, **450**, 3665
- Sereno, M., & Ettori, S. 2017, *MNRAS*, **468**, 3322
- Shapley, A. E., Steidel, C. C., Strom, A. L., et al. 2016, *ApJL*, **826**, L24
- Sharon, K., Gladders, M. D., Rigby, J. R., et al. 2012, *ApJ*, **746**, 161
- Smit, R., Bouwens, R. J., Camiani, S., et al. 2018, *Natur*, **553**, 178
- Smith, G. P., Mazzotta, P., Okabe, N., et al. 2016, *MNRAS*, **456**, L74
- Stacey, G. J., Hailey-Dunsheath, S., Ferkinnhoff, C., et al. 2010, *ApJ*, **724**, 957
- Stark, D. P. 2016, *ARA&A*, **54**, 761
- Stark, D. P., Ellis, R. S., Charlot, S., et al. 2017, *MNRAS*, **464**, 469
- Stark, D. P., Ellis, R. S., Chiu, K., Ouchi, M., & Bunker, A. 2010, *MNRAS*, **408**, 1628
- Stark, D. P., Richard, J., Charlot, S., et al. 2015, *MNRAS*, **450**, 1846
- Stark, D. P., Richard, J., Siana, B., et al. 2014, *MNRAS*, **445**, 3200
- Strolger, L.-G., Dahlen, T., Rodney, S. A., et al. 2015, *ApJ*, **813**, 93
- Sunyaev, R. A., & Zeldovich, Y. B. 1970, *Ap&SS*, **7**, 3
- Tamura, Y., Mawatari, K., Hashimoto, T., et al. 2019, *ApJ*, **874**, 27
- Tilvi, V., Papovich, C., Finkelstein, S. L., et al. 2014, *ApJ*, **794**, 5
- Tokunaga, A. T., & Vacca, W. D. 2005, *PASP*, **117**, 421
- Treu, T., Brammer, G., Diego, J. M., et al. 2016, *ApJ*, **817**, 60
- Treu, T., Schmidt, K. B., Brammer, G. B., et al. 2015, *ApJ*, **812**, 114
- Treu, T., Schmidt, K. B., Trenti, M., Bradley, L. D., & Stiavelli, M. 2013, *ApJL*, **775**, L29
- Umetsu, K., Broadhurst, T., Zitrin, A., Medezinski, E., & Hsu, L. 2011, *ApJ*, **729**, 127
- Umetsu, K., Medezinski, E., Nonino, M., et al. 2014, *ApJ*, **795**, 163
- Umetsu, K., Zitrin, A., Gruen, D., et al. 2016, *ApJ*, **821**, 116
- van Weeren, R. J., Röttgering, H. J. A., Intema, H. T., et al. 2012, *A&A*, **546**, A124
- Vanzella, E., Nonino, M., Cupani, G., et al. 2018, *MNRAS*, **476**, L15
- Vega-Ferrero, J., Diego, J. M., Miranda, V., & Bernstein, G. M. 2018, *ApJ*, **853**, L31
- von der Linden, A., Allen, M. T., Applegate, D. E., et al. 2014a, *MNRAS*, **439**, 2
- von der Linden, A., Mantz, A., Allen, S. W., et al. 2014b, *MNRAS*, **443**, 1973
- Watson, D., Christensen, L., Knudsen, K. K., et al. 2015, *Natur*, **519**, 327
- Wen, Z. L., Han, J. L., & Liu, F. S. 2012, *ApJS*, **199**, 34
- Windhorst, R. A., Timmes, F. X., Wyithe, J. S. B., et al. 2018, *ApJS*, **234**, 41
- Wittman, D., Golovich, N., & Dawson, W. A. 2018, *ApJ*, **869**, 104
- Wong, K. C., Zabludoff, A. I., Ammons, S. M., et al. 2013, *ApJ*, **769**, 52
- Wright, E. L., Eisenhardt, P. R. M., Mainzer, A. K., et al. 2010, *AJ*, **140**, 1868
- Wuyts, S., Labbé, I., Schreiber, N. M. F., et al. 2008, *ApJ*, **682**, 985
- Zheng, W., Postman, M., Zitrin, A., et al. 2012, *Natur*, **489**, 406
- Zitrin, A., Broadhurst, T., Umetsu, K., et al. 2009, *MNRAS*, **396**, 1985
- Zitrin, A., Fabris, A., Merten, J., et al. 2015a, *ApJ*, **801**, 44
- Zitrin, A., Labbé, I., Belli, S., et al. 2015b, *ApJL*, **810**, L12
- Zitrin, A., Seitz, S., Monna, A., et al. 2017, *ApJL*, **839**, L11
- Zitrin, A., Zheng, W., Broadhurst, T., et al. 2014, *ApJL*, **793**, L12